Mesospheric nitric acid enhancements during energetic electron precipitation events simulated by WACCM-D

Yvan J. Orsolini[1,2], Christine Smith-Johnsen[3,2], Daniel R. Marsh[4], Frode Stordal[3], Craig J. Rodger[5], Pekka T. Verronen[6] and Mark A. Clilverd[7]

[1]NILU - Norwegian Institute for Air Research, Kjeller, Norway.

[2]Birkeland Centre for Space Science, University of Bergen, Norway.

[3]Department of Geosciences, University of Oslo, Oslo, Norway.

[4]NCAR, Boulder, USA.

[5]Department of Physics, University of Otago, Dunedin, New Zealand.

[6]Space and Earth Observation Centre, Finnish Meteorological Institute, Helsinki, Finland

[7]British Antarctic Survey, Cambridge, UK.

Corresponding author: Yvan J. Orsolini (yvan.orsolini@nilu.no)

Key Points:

- D-layer ion chemistry enhances production of mesospheric nitric acid through ion cluster recombination with a seasonal maximum in winter
- Medium-to-high energy electrons precipitating into the mesosphere in April-May 2010 further enhances the formation of nitric acid
- Occurring at a time of year with low background abundance, the enhancement brought nitric acid abundance close to its annual cycle maximum

Abstract

While observed mesospheric polar nitric acid enhancements have been attributed to energetic particle precipitation through ion cluster chemistry in the past, this phenomenon is not reproduced in current whole-atmosphere chemistry-climate models. We investigate such nitric acid enhancements resulting from energetic electron precipitation events using a recently developed variant of the Whole Atmosphere Community Climate Model (WACCM) that includes a sophisticated ion chemistry tailored for the D-layer of the ionosphere (50-90 km), namely WACCM-D. Using the specified-dynamics mode, i.e., nudging dynamics in the troposphere and stratosphere to meteorological re-analyses, we perform a one-year long simulation (July 2009-June 2010) and contrast WACCM-D with the standard WACCM. Both WACCM and WACCM-D simulations are performed with and without forcing from medium-to-high energy electron precipitation, allowing a better representation of the energetic electrons penetrating into the mesosphere. We demonstrate the effects of the strong particle precipitation events which occurred during April and May 2010 on nitric acid and on key ion cluster species, as well as other relevant species of the nitrogen family. The one-year-long simulation allows the event-related changes in neutral and ionic species to be placed in the context of their annual cycle. We especially highlight the role played by medium-to-high energy electrons in triggering ion cluster chemistry and ion-ion recombinations in the mesosphere and lower thermosphere during the precipitation event, leading to enhanced production of nitric acid and raising its abundance by two orders of magnitude from 10^{-4} to a few 10^{-2} ppb.

1 Introduction

Nitric acid (HNO_3) is an important minor species in the middle atmosphere. Over the last decades, its distribution has been characterized by means of ground-based, aircraft and satellite observations at infrared and millimetre wavelengths [e.g., de Zafra and Smyshlaev, 2001; Santee et al., 2004; Orsolini et al., 2005, 2009; Stiller et al., 2005; Kinnisson et al., 2008; Verronen et al., 2008, 2011; Urban et al., 2009; Damiani et al., 2016]. HNO_3 is most abundant in the polar lower stratosphere in winter, where its long lifetime during the dark conditions makes it a key reservoir of reactive nitrogen (NOx = NO+NO_2), which drives the main ozone-depleting cycle in the mid and upper stratosphere. Yet, satellite observations have revealed descent of HNO_3 from above the upper stratosphere, leading to the formation of a secondary maximum, well above the main lower stratospheric layer. These recurrent enhancements are observed in the polar regions of both hemispheres with a large degree of inter-annual variability, and they have been linked to energetic particle precipitation (EPP), the main source of NOx in the mesosphere-lower thermosphere (MLT). Satellite and ground-based observations are often limited to the stratosphere due to retrieval constraints, but occasional mesospheric HNO_3 enhancements have been documented during solar proton events (SPEs) [Verronen et al., 2011], when larger abundances expand vertically the validity range of the retrievals.

Both SPEs and energetic electron precipitation (EEP) lead first to the formation of primary ions such as O^+, O^+_2, N^+_2, and N^+ through dissociation and dissociative ionisation. These ions are then involved in fast ion-chemistry reactions, ultimately producing NOx and hydrogen oxides (HOx) (e.g., see Sinnhuber et al., 2012 for a review). The chemistry of ion clusters plays a key role in the production of the neutral nitrogen species. Ion clusters are groups of *m* molecules tied to a positive or negative ion. For example, *m* water molecules can form the hydrated water cluster $H^+(H_2O)_m$, or else other water clusters like $NO_3^-(H_2O)_m$ or $NO^+(H_2O)_m$. The number *m*, the order

of the cluster, indicates the attachment of *m* molecules. Another important ion cluster group for the production of HNO_3 which was identified in previous studies (Verronen et al., 2011; Andersson et al., 2016) is the nitric acid cluster $NO_3^-(HNO_3)_m$, i.e., *m* HNO_3 molecules attached to the negative NO_3^- ion.

With only a few exceptions, the EPP-related upper stratospheric/mesospheric source of HNO_3 is not accounted for in middle atmosphere global models, as they do not incorporate the relevant ion chemistry. Reddmann et al. (2010) included a parametrization of HNO_3 hydrolysis in a chemistry transport model, focusing on the aftermath of the SPE of October 2003. Kvissel et al. (2012) used the same approach, along with an idealised background distribution of hydrated water clusters, in simulations using the free-running Whole Atmosphere Community Climate Model (WACCM). In addition to producing wintertime enhancements of HNO_3, the latter study showed complex chemical-dynamical feedbacks, which extended the effect of the EPP-induced winter increase of NOx into the warm season by weakening the polar vortex and enhancing the poleward transport of NOx from lower latitudes. The vortex weakening (when the parametrized ion chemistry reaction was included) arose from strengthened planetary waves due to zonal asymmetries in ozone induced by enhanced NOx anomalies.

It is apparent that ion chemistry needs to be taken into account to correctly represent the observed distribution of HNO_3, and also that this chemistry could exert a potential feedback on ozone and dynamics. Hence, a more comprehensive ion chemistry is needed to account for the effect of EPP *on neutral species* in models. Previous studies with comprehensive ion chemistry were limited to one-dimensional (1-D) models, which at best only crudely represent transport. For example, Verronen et al. (2011) investigated the chemistry involved in the HNO_3 enhancements during the SPEs of January 2005 and December 2006. They compared the results from the comprehensive 1-D Sodankylä Ion and Neutral Chemistry (SIC) model with satellite observations from the Microwave Limb Sounder (MLS) instrument at the highest sampled latitudes, where horizontal mixing was assumed to be small. The same model was used to analyse the chemical impact of EPP during pulsating auroras (Turunen et al., 2016).

Very recently, an extended ion chemistry based on a subset of reactions and species from the comprehensive SIC model has been incorporated into the global chemistry-climate model WACCM. This variant of WACCM called WACCM-D, where D stands for the D-layer of the ionosphere (below the mesopause), is described in detail by Verronen et al. (2016). Andersson et al. (2016) investigated the chemical effects of the SPE of 2005, in particular on HNO_3, and showed that the production of HNO_3 increased by two orders of magnitude between 40 and 70 km, bringing WACCM-D closer to the MLS satellite observations.

The aim of this paper is to investigate, through a case study, the effect of EEP events on the distribution of HNO_3 and relevant ion clusters in the new WACCM-D model in comparison to the standard WACCM, in the presence of medium-to-high energy electron (MEEs) forcing. We analyse a series of events which took place in April and May 2010, the first in a series of moderate geomagnetic storms that perturbed the upper atmosphere from April to July 2010 (Kirkwood et al., 2015). Our focus is on the high-latitude mesosphere and lower thermosphere. Hence, our study differs from the above-mentioned studies with WACCM-D in that we investigate EEP events rather than a SPE. Our simulation also covers an entire year rather than

the weeks around the precipitation event, allowing us to examine the EEP events in the context of the seasonal variations of neutral and ionic species.

2. The WACCM-D simulations and ancillary data

We use the WACCM-D model jointly developed by researchers from the National Center for Atmospheric Research (NCAR) and the Finnish Meteorological Institute (FMI) (Verronen et al., 2016; Andersson et al., 2016). WACCM-D is a recent development of WACCM (version 4), a global circulation model with fully coupled chemistry and dynamics, which extends from the surface to ~145 km (with 88 pressure levels in total). The ion chemistry in WACCM-D, with 20 positive ions, 21 negative ions and 307 reactions, includes a selected subset of ionic species and reactions based on the analysis of Verronen and Lehmann (2013), and it has been shown to produce a representation of the D-region ionosphere very similar to the more comprehensive but 1-D SIC model (Verronen et al. 2016). The selected additional ionic species were added to 5 pre-existing ones in the standard WACCM (O^+, NO^+, O^+_2, N^+_2, N^+).

The EPP-related production of HOx and NOx which is parametrized in WACCM is, importantly, replaced by the ionic chemical reactions. The reader is referred to the two above-mentioned papers for an exhaustive description of WACCM-D, and to Marsh et al. (2007) for the MLT representation in the standard WACCM. Our simulations with WACCM-D or the standard WACCM are mostly inter-compared in terms of the *ratio* (WACCM-D divided by WACCM) in key minor constituents. Only in section 3.3 will the absolute differences be used. All simulations have been performed with enhanced eddy diffusion, using a Prandtl number of 2 (Garcia et al., 2014). Galactic cosmic rays are also accounted for in these simulations.

Note also that all the simulations described in the current study are in specified dynamics (SD-WACCM) mode (e.g., Marsh, 2011), i.e. nudged up to about 0.79 hPa toward the Modern-Era Retrospective Analysis for Research and Application (MERRA) reanalysis of NASA's Global Modelling and Assimilation Office (Rienecker et al., 2011). Above this level (i.e., in the region where the ion chemistry is particularly active), SD-WACCM transitions linearly to a free running model. For brevity, we omit the "SD-" prefix, and refer simply to WACCM and WACCM-D, although we use the specified dynamics mode throughout this paper. Our simulations were made at a horizontal resolution of 1.9°×2.5° (latitude × longitude), cover the period July 2009 to June 2010, and were initialised from existing WACCM initial states. We particularly examine the period spanning April to May 2010 using daily-mean data, although the annual cycle from July 2009 to June 2010 will also be shown using monthly-mean data.

The parameterization of auroral electron precipitation in WACCM has been supplemented by the inclusion of additional ionisation due to MEEs. The details on the derivation of the MEE fluxes and the calculation of the associated ionization rates are given in the Appendix. Having twin simulations with and without MEEs allows us to separate the contributions to the HNO_3 enhancement from the D-region ion chemistry from the MEE forcing. We focus on high latitudes where EEP is concentrated, and thus undertake polar averaging over all latitudes poleward of 50° to include the full meridional extension of the auroral ovals. In total, we carried out four simulations, i.e., with and without ion chemistry (WACCM-D or WACCM), and with and without the MEE forcing.

We examine the distribution of HNO_3 and of the following four key ion cluster groups: the water clusters $H^+(H_2O)_n$ (with n=1,5), $NO^+(H_2O)_n$ (with n=1,3), $NO_3^-(H_2O)_n$ (with n=1,2), and the nitric acid ion cluster $NO_3^-(HNO_3)_n$ (with n=1,2). Our model output is for an ion cluster group, i.e. for all n and not for individual cluster orders. The individual ion clusters are treated as prognostic species only in WACCM-D, and are not included in the standard WACCM. Although individual ion clusters are short-lived, their abundances adjust to the transport and chemical production or loss of their longer-lived source species. In the thermosphere, the abundances of ion clusters become very low, and it is expected that the ion chemistry is driven by the 5 primary ions already included in WACCM.

The geomagnetic storm period of April 2010 was driven by a combination of both co-rotating interaction regions associated with high-speed solar wind streams and of coronal mass ejections associated with dense transient solar wind flows. This period is also described in more detail in Smith-Johnsen et al. (2017). We use the Disturbance Storm Time (Dst) index to characterise the storm onset and evolution. The minimum of -81 nT (nanoTesla) on the 5th of April classifies it as a moderate geomagnetic storm. The recovery period is interrupted by a second moderate geomagnetic storm (with Dst of -67 nT) on the 12th of April. Further storms of similar magnitudes, in term of Dst deflections, occurred in early May and June of that year. There were no large solar proton events during the simulated year.

3. Results

3.1. Annual evolution

3.1.1 Monthly mean polar-averaged HNO_3 distributions

The monthly-mean, polar-averaged (zonally and over latitudes poleward of 50 degree) evolution of HNO_3 throughout the modelled year (July 2009 to June 2010) from 40 to 110 km altitude is shown in Figure 1 for standard WACCM and for WACCM-D, as well as their ratio (WACCM-D divided by WACCM), for both hemispheres. In both WACCM and WACCM-D, there is a seasonal march in the HNO_3 abundance, which culminates in the winter months (e.g., June-July in the SH, in this case July 2009 and June 2010, and December-January in the NH, in this case December 2009 and January 2010). Inspection of the ratio shown in the lowest panels reveals that the abundance of HNO_3 is increased by over two orders of magnitude in WACCM-D in the altitude range 55-75km, pointing to the important role of ion chemistry in producing mesospheric HNO_3. The ratio is most strongly amplified in April-May 2010 in both hemispheres, raising abundances from 10^{-4} to a few 10^{-2} ppb and suggesting that the EEP events may play a role then. Above 90 km, the background abundance of HNO_3 is very low in both models, but the increase in the ratio in April-May 2010 remains substantial throughout the lower thermosphere (over a factor 10) in both hemispheres, although weaker than for the altitudes below. We will return to this influence of the precipitation events in section 3.2.We further note that, in the upper stratosphere, there is no large increase even though the ion chemistry could have been, in principle, active in the cold winter conditions.

Figure 2 (left panel) shows the monthly-mean seasonal cycle of HNO_3 averaged in the polar caps (poleward of 50 degrees latitude) in both hemispheres, and averaged over an altitude range of 70-

75 km. It reveals a peak-to-peak variation in the seasonal cycle that is twice as large in the SH as in the NH, and a maximum abundance in winter (0.07 ppb in the SH and 0.035 ppb in the NH).

3.1.2 Chemical pathways for HNO_3 production

Up to now, we have not yet discussed which pathways of ion or neutral chemistry described in Verronen and Lehmann (2013) are the most important for the production of HNO_3 in WACCM or WACCM-D. In the standard WACCM, there is some weak HNO_3 production (Fig. 1) arising from the neutral reaction

$NO_2 + OH + M \rightarrow M + HNO_3$

WACCM-D however includes the key ion-ion recombination reactions between water ion clusters and the nitric acid ion clusters, that produce HNO_3:

(reaction pathway R1 : ion-ion recombination reactions forming HNO_3)

$H^+(H_2O)_n + NO_3^-(HNO_3)_m \rightarrow (m+1)\ HNO_3 + n\ H_2O$

$NO^+(H_2O)_n + NO_3^-(HNO_3)_m \rightarrow NO + NO_3 + m\ HNO_3 + n\ H_2O$

Another set of ionic reactions involved in the production of HNO_3 in the stratosphere is the conversion of N_2O_5 into HNO_3 through a hydrolysis reaction involving hydrated water clusters (Kawa et al., 1995; Kvissel et al., 2012 and references therein):

(reaction pathway R2: hydrolysis of N_2O_5)

$H^+(H_2O)_n + N_2O_5 \rightarrow H^+(H_2O)_{n-1}(HNO_3) + HNO_3$

$H^+(H_2O)_{n-1}(HNO_3) + H_2O \rightarrow H^+(H_2O)_n + HNO_3$

This reaction pathway (R2) sequesters NOx from the N_2O_5 reservoir into the longer-lived HNO_3 reservoir, and mostly plays a role in the stratosphere, since the abundance of N_2O_5 falls rapidly with height in the upper stratosphere and mesosphere.

Figure 3 compares the winter-mean vertical profiles of several (neutral) nitrogen species between WACCM and WACCM-D, in each hemisphere. We first remark that the winter increase in WACCM-D is found not only in HNO_3 but also in NO_3 and to a much smaller extent in N_2O_5. HNO_3 is enhanced above 40 km altitude. The NO_3 production is not very efficient in the mesosphere and its background level is very low. As seen on Fig. 3, NO_3 is only very weakly enhanced below 65 km and strongly enhanced between 70 and 85 km. Ion-ion recombination reactions involving the several types of water ion clusters can explain - through ion chemistry- the increase in NO_3 by up to two orders of magnitude (from 10^{-6} to 10^{-4} ppb) in WACCM-D compared to WACCM. Such reactions include

$H^+(H_2O)_n + NO_3^-(H_2O)_m \rightarrow H + NO_3 + (n+m)\ H_2O$

$NO^+(H_2O)_n + NO_3^-(H_2O)_m \rightarrow NO + NO_3 + (n+m)\ H_2O$

$NO^+ + NO_3^-(H_2O)_n \rightarrow NO + NO_3 + n\ H_2O$

Ion chemistry also enhances the NOx production compared to the parameterisation used in standard WACCM (Andersson et al. 2016), which is another factor relevant to the increased NO_3

through neutral chemistry. N_2O_5 also increases only very weakly below 65 km; the increase is larger above 70 km, though still smaller than that for NO_3. The increase in this case is consistent with the neutral reaction

$NO_2 + NO_3 + M \rightarrow M + N_2O_5$

and the N_2O_5 increase is limited to the layer where NO_3 is produced by the ion-ion recombination in WACCM-D. In short, the hydrolysis of N_2O_5, pathway R2, is unimportant for the seasonal production of HNO_3 due to the small abundance of N_2O_5 in the mesosphere, itself tied to NO_3 (Fig. 3).

3.1.3 Monthly mean polar-averaged distributions of ion clusters

The corresponding seasonal evolution of the four ion cluster species is shown in Fig. 4. The abundances vary with season and height. The $H^+(H_2O)_n$ and $NO^+(H_2O)_n$ water clusters have a maximum abundance in summer. This seasonal-dependence and its height variation follows the seasonal march of water vapour abundance as indicated by two white contours on Fig. 4, corresponding to 2 and 5 ppmv, with the summer-to-winter pole meridional circulation in the mesosphere bringing up air enriched in water vapour at high latitudes in summer, and bringing down dry air in winter. The $NO_3^-(H_2O)_n$ water cluster and the nitric acid cluster $NO_3^-(HNO_3)_n$ tend to maximize in winter, indicating that the abundance of NO_3^- is, in this case, the limiting factor. A higher abundance of NOx has been previously reported in the winter high latitudes due to the descent from the MLT (e.g., Randall et al., 2007). This coincidence in time between higher abundance of precursory NOx and the secondary winter maximum in $H^+(H_2O)_n$, weaker than the summer one and occurring when abundance of water vapour is low, is suggestive of a role for conversion of $NO^+(H_2O)_n$ to $H^+(H_2O)_n$ (Verronen and Lehmann, 2013).

3.2 Changes around the April and May geomagnetic storms

3.2.1 Daily polar-averaged HNO_3 distributions

The period of April and May 2010 is characterised by large enhancements in mesospheric and lower thermospheric HNO_3 in WACCM-D, following the Dst negative excursions that mark the occurrences of the storms. The daily-averaged, polar-averaged abundances in WACCM-D (Fig. 5) are higher than in WACCM by over two orders of magnitude. Close inspection of the ratio indicates that the short-lived relative enhancements clearly appear in bursts. These bursts are tied to the Dst fluctuations but also, in the mesospheric layer at 50-70 km in particular, the daily-varying increases related to the geomagnetic storms are superimposed on a seasonal cycle variation. In the SH, the daily-varying enhancements also occur when the HNO_3 abundance is increasing as the winter approaches, while it is decreasing in the NH (see Fig. 1).

Returning to Fig. 2 (right panel), we note that the HNO_3 increase due to the April 2010 EEP event in WACCM-D is much smaller than the corresponding increase after the January 2005 SPE, discussed by Andersson et al. (2016). They found an increase in HNO_3 of 0.5-1.0 ppb near 70-75 km during the SPE (their Figure 9, top panel) in the NH. By contrast, Fig. 2 (right panel) shows that, in the SH, the increase during the EEP events has a maximum value of 0.075 ppb near 70-75 km in WACCM-D, at the peak of the events. It is hence a factor 5 to 10 smaller than for the SPE. In the NH, the HNO_3 increase is only about 0.005 ppb, i.e. 20 times smaller than in

the SH. It is important to note that SPEs are comparatively rare events, while MEE electron precipitation is considerably more common. The EEP event occurred at a time of year (April) when background abundances of HNO_3 are low in both hemispheres (Fig. 2, left panel), but the abrupt increase in the austral polar cap during the EEP event brings HNO_3 close to its seasonal maximum.

3.2.2 Daily polar-averaged distributions of ion clusters.

The corresponding day-to-day evolution of the abundance of the 4 ion cluster species (Fig. 6) is marked by an abrupt increase in most of the clusters following the Dst negative excursions indicating storm onsets. While Fig. 4 had shown that the $H^+(H_2O)_n$ abundance followed the seasonal H_2O cycle, it is clear from Fig. 6 that the rapid enhancements during the EEP events occur in the declining phase of water vapour abundance in the SH or in its slowly increasing phase in the NH (see the white contours). Enhancements of hydrated water cluster ions during the EEP event are due to higher ionisation and higher abundances of ions, including precursory $NO^+(H_2O)_n$ ion clusters or also oxygen ion clusters $O_2^+(H_2O)_n$, followed by the conversion to $H^+(H_2O)_n$ (Verronen and Lehmann, 2013).

In Fig. 7, we also compare the changes in WACCM-D during the EEP event, i.e., contrasting the quiet and active periods (April 1-3 and April 6-8, respectively), for the aforementioned three neutral species and the four key ion clusters. Starting with the neutral species, the changes during the event are qualitatively similar to those seen during the seasonal cycle. The layer where HNO_3 increases is somewhat narrower for the EEP-related changes than for the changes due to the seasonal cycle, since the latter are also influenced by transport, due to the longer time scales involved. Since the event took place in April, the abundance of N_2O_5, which is easily photo-dissociated, is smaller in the NH, which is more sunlit in boreal spring conditions. Again, the N_2O_5 change is constrained by the increase in NO_3 produced by the ion cluster chemistry during the EEP event. Turning now to the ion clusters and their changes between the quiet and active period, we again notice how their respective abundances decrease sharply with increasing altitude, reflecting the decreasing availability of H_2O or HNO_3, as seen earlier (Fig. 4). Above 90 km, the $NO^+(H_2O)_n$ ion cluster becomes the most abundant, reflecting the primary importance of the NO^+ ion in the thermosphere. It is apparent that the additional production of HNO_3 and NO_3 between the quiet and active period is tied to the enhanced abundances of the various ion clusters in WACCM-D, which recombine in ion-ion reactions. For example, NO_3 is decreasing sharply above 80 km along with the two ion clusters tied to the negative ion NO_3^-. Also, the lower boundary of the HNO_3 increase near 55 km is tightly constrained by the altitude where the abundance of hydrated ion water clusters starts to increase due to the influence of energetic electrons (this will be even clearer in Fig. 12). In short, these figures are consistent with ion cluster recombinations (R1) playing the dominant role in the formation of HNO_3 during the EEP event.

3.2.3 Geographical maps of nitric acid and ion cluster abundances

We focus hereafter on the changes in the geographical distribution of HNO_3 at 70 km between the pre-storm quiet period (a 3-day period, April 1-3) and the active storm period (a 3-day period, April 6-8). These are shown as geographic maps in Figs 8 and 9 for the NH and the SH, respectively. We chose the early April storm since it is easier to contrast to the quiet pre-storm conditions, but the same changes are seen in the simulations for the May event (not shown). It is

apparent that there is already some enhancement in WACCM-D compared to WACCM within most of the whole polar cap even during the quiet period, related to the seasonal cycle enhancement in WACCM-D, albeit at much lower levels than during the time of the storm. The changes between the active and quiet periods are already present in WACCM (see Fig. 5), but the amplification is stronger and much more widespread in WACCM-D, up to 10^{-2} rather than to 10^{-3} ppb. In the active period, HNO_3 increases considerably along the oval regions, i.e., in the region symmetric in geomagnetic coordinates which experiences enhanced ionisation (see Appendix). The equatorward expansion of the ovals at the initiation of the storm can be noticed in the enhancements on the equator-side of the pre-storm oval edges (Figs. 8-9). The increase is stronger in the SH, as had been shown earlier in Fig. 2.

The geographical distributions of the 4 ion cluster species at 70 km (Figs. 10 and 11) readily illustrate the enhancements of the ion cluster distributions along the ovals during the EEP event. That is, the chemical effect of EEP is not limited to NOy species and the enhancements in ion clusters play an important role as outlined in section 3.1.2. The distribution of the ion cluster containing the NO_3^- ion is more complex than the water ion clusters. The ion clusters are short-lived but their distributions reflect the changing distributions of precursory neutral species, like NO_2 in the case of the NO_3^- ion clusters. It is also apparent from Figs. 8-11 that, while HNO_3 and ion clusters remain close to their production around the auroral oval in the NH, they are more readily redistributed within the polar cap in the SH. The inter-hemispheric differences, namely that the changes are confined to a narrow latitude band characteristic of the auroral oval in the NH, but spread into the polar cap in the SH, can be explained by the larger oval offset (i.e., difference in the zonal direction between the magnetic and geographic coordinate systems) in the SH. Hence, in the SH, there is a tendency for the zonal winds to rapidly redistribute species with isopleths along magnetic coordinates. Also, the NH is more sunlit at this time of the year and NO and HNO_3 are more readily photolysed. The transport by the mean meridional circulation is stronger in April-May in the SH (during austral fall) than in the NH (during boreal spring) (e.g., Smith et al., 2015). The inter-hemispheric differences during the EEP event, with stronger polar cap-averaged abundances of HNO_3 or ion clusters in the SH, can also be seen in the profiles shown in Figs. 7.

3.3 Role of the MEE ionization

Since the aim of this paper was to examine an energetic electron precipitation event, it appears sensible to include the forcing by medium-to-high energy electrons (MEE). The previous figures hence showed results from WACCM or WACCM-D simulations with the MEEs included. In this section, we nevertheless compare those simulations with simulations where the MEE forcing is removed, leaving only auroral electron precipitation, in order to delineate more specifically the effect of this MEE precipitation.

Covering the period around the EEP event, Figure 12 shows the April-mean zonally averaged meridional-height cross sections of HNO_3 from both WACCM and WACCM-D, with and without the inclusion of MEEs, as well as their absolute differences. Hence, the differences between the plots along a row (i.e., (b)-(a) or (e)-(d)) indicate the change due to the introduction of the MEEs in WACCM or WACCM-D, while the differences along a column (i.e., (d)-(a) or (e)-(b)) indicate the changes due to the introduction of the D-region ion chemistry. From Fig. 12c, it is clear that, in the standard WACCM, the MEEs produce little change in HNO_3 in the

upper stratosphere or MLT region. It is only with the inclusion of the ion chemistry in WACCM-D that the EEP-induced production of HNO_3 is amplified (Fig. 12f). Although there is already a mesospheric and thermospheric HNO_3 increase in WACCM-D without the MEEs, it is further increased by the inclusion of that precipitation. This is an indication that energetic electrons, which penetrate deeper into the mesosphere region, further trigger the ionic reactions which produce HNO_3. Figure 12i contrasts the simplest and the most elaborate model, i.e., the standard WACCM without MEE and WACCM-D with MEE. Figure 12 hence stresses the important role played by MEEs during the event: in the absence of MEEs, the HNO_3 enhancements in WACCM-D are much weaker. To further stress the important triggering role played by particle precipitation and by MEE in particular on the HNO_3 production during the event, Fig. 13 compares the two versions of WACCM-D, with and without MEE, at the peak of the EEP event (April 6-8). Importantly, the abundances of the four key ion clusters clearly increase in the mesosphere with the inclusion of the MEEs above 55 km, which is consistent with the strong increase of the HNO_3 production by MEE demonstrated in Fig. 12.

Finally, returning to Fig. 2 (left panel; red lines), we can see that the forcing by MEEs is strengthening the seasonal cycle in both hemispheres outside of the period of large negative Dst fluctuations in April and May 2010.

4. Summary

In summary, EPP induces the formation of ion clusters, and the ion-ion recombinations (reaction pathway R1) between these clusters lead to the production of HNO_3. Our study of an EEP event indicates that the effect is 5 to 10 times smaller than during a SPE event, but the event occurred at a time of year when the seasonally varying background of HNO_3 is low. Our study also confirms the importance of the ion-ion recombination pathway (R1) over the hydrolysis of N_2O_5 (R2), as shown by Verronen et al. (2001) during SPEs. NO_3 is also produced by similar ion-ion recombinations. There is a seasonal component of this HNO_3 production, independent of the EEP event, which is stronger in WACCM-D compared to WACCM due to the background presence of ion clusters, and which is stronger in WACCM-D with the inclusion of MEE. Superposed on this seasonal cycle, the EEP event considerably augments the production of HNO_3 raising its abundance by two order of magnitude from 10^{-4} to a few 10^{-2} ppb. This effect is enhanced by the inclusion of the MEE, allowing more production of the necessary ion clusters down to 55 km in the latitude bands characteristic of the auroral ovals.

Three-dimensional middle atmospheric modelling with ion chemistry models such as WACCM-D is in its infancy, and only the aforementioned handful of studies have been published in the last year. Such model simulations with WACCM-D open new possibilities to study the connection between the neutral middle-atmosphere and the D-region ionosphere. It has been already shown by Andersson et al. (2016) that the ion chemistry in WACCM-D lead to a better agreement with satellite observations of HNO_3, HOx and NOx during SPEs. Further studies of the short and long-term variability in mesospheric HNO_3 using satellite observations (e.g., from MLS, Michelson Interferometer for Passive Atmospheric Sounding (MIPAS), Atmospheric Chemistry Experiment-Fourier Transform Spectrometer (ACE-FTS), or other instruments) would be warranted in order to support the conclusions of this model study. This would however require that satellite retrievals are improved and validated in the mesosphere. It should be also

noted that WACCM-D ion chemistry can provide a realistic electron density also in the lower ionosphere (Verronen et al., 2016), so that comparison against ionospheric observations such as ground-based radars can be used to study, e.g., the quality of the simulated EPP forcing. Further work with WACCM-D can be made to test our overall understanding of important ions and their reactions, both in the MLT and the stratosphere.

Appendix : Producing the MEE forcing

The energetic electron precipitation (EEP) forcing applied in the current study was developed as part of an effort to include EEP in climate models, such as WACCM. The approach used here is based on direct satellite measurements. By contrast, recent efforts undertaken to produce the EEP forcing as part of the solar forcing dataset recommended for CMIP6, as described in van de Kamp et al. (2016) or Matthes et al. (2017), rely on a proxy-based parametrization in order to extend the series back in time, prior to the satellite era.

The energetic electron precipitation flux was determined from the experimental measurements made from 1998-2012 by the Space Environment Monitor 2 (SEM-2) instrument packages onboard the constellation of Polar Orbiting Environment Satellites (POES). The POES are a long-lived series of spacecraft in Sun-synchronous high-inclination orbits at roughly 800-850 km altitude. Included in the POES SEM-2 instrument is the Medium Energy Proton and Electron Detector (MEPED) and the Total Energy Detector (TED) that together monitor electron fluxes over the nominal energy range from 50 eV to 2.5 MeV (Evans and Greer, 2004; Rodger et al., 2010a). Here we focus on the electron fluxes observed by the 0^0 MEPED telescope, as this principally measures electrons with pitch angles inside the Bounce Loss Cone (Rodger et al., 2010b), which will be lost locally on short time scales (i.e., on the order of seconds). Observations from this telescope can provide an indication of the EEP input into the atmosphere at a location joined by the geomagnetic field line to the satellite in question. During the period studied here, up to 6 distinct SEM-2 carrying satellites were operational simultaneously (see Table 2 of Neal et al. (2013) for a list with summary information), each of which had orbital periods of ~100 min.

The MEPED electron observations are of integral electron counts for the nominal energy ranges >30 keV (e1), >100 keV (e2), and >300 keV (e3). Previous studies have identified significant contamination in the electron channels by protons with energies of hundreds of keV (Yando et al., 2011). Unfortunately, such protons can reach considerable levels during geomagnetic storms, which is also when EEP is likely to be most active. We correct for this proton contamination by applying a NOAA-developed algorithm (Lam et al., 2010), validated by Whittaker et al. (2014). In addition, solar proton events and the high-energy protons in the South Atlantic Magnetic Anomaly are known to swamp the electron detectors, leading to no meaningful electron measurements. Hence, all solar proton event periods, as well as observations from inside and around the South Atlantic Magnetic Anomaly, are excluded. We note that for the period studied in this paper, there were no data excluded due to solar proton events.

The original MEPED electron observations have 2 s resolution. In order to produce long-term EEP fluxes, the electron observations from each integral channel were combined from all operational POES instruments by zonally averaging the measurements in geomagnetic coordinates with 3 hour time resolution and 0.5 L resolution (where L is the McIlwain L-

parameter (McIlwain, 1961)). We restrict ourselves to the *L* range from 2.25-9.75, which encompasses the outer radiation belt. It has previously been shown that power-laws are an accurate representation of the EEP flux spectrum, i.e., through a comparison of high energy resolution DEMETER electron flux observations with POES MEPED measurements (Whittaker et al., 2013). Hence, we fit a powerlaw spectrum to the three 0° electron telescopes (e1, e2, e3) to obtain the energy spectral gradient (*k*) for the precipitating electrons.

Unfortunately, the small angular size of the MEPED/POES telescope results in low sensitivity at lower flux magnitudes (Yando et al., 2011), which causes the MEPED electron observations to have a comparatively high minimum detectable flux (~10^2 el.cm^{-2} s^{-1} sr^{-1} in each integral channel). Due to experimental noise, periods with lower EEP fluxes may appear to have near constant EEP at this minimum detectable level, although they have been shown to be inconsistent with other experimental datasets (e.g., Neal et al., 2015). So as not to bias the fluxes during the relatively common situation of geomagnetic quiet times (when EEP levels are likely near-zero), we set all EEP flux magnitudes <250 cm^{-2} s^{-1} sr^{-1} to zero. The near noise-level fluxes can also produce artificially hard power law spectra; we therefore limit $k<-1$, and set any periods with $k\geq-1$ to $k=-1$. Finally, we follow Rodger et al. (2013) and remove all electron observations when the MEPED P7 omni-directional detector reports >36 MeV protons, i.e. set them to zero. This should suppress the impact of solar proton event contamination. However, is important to note that this means the EEP flux representation provided here will not be fully accurate during solar proton events, where no meaningful experimental measurements of EEP are available from POES.

The combination of these processes should ensure that unrealistically high levels of EEP are excluded during quiet times or during solar proton events, an issue that has been identified in other EEP products derived from POES electron observations (e.g., Neal et al., 2015).

The power-law fitted EEP parameters were then used to determine ionization rates assuming the EEP had a differential power-law flux spectrum covering the energy range from 50 keV - 2 MeV using 78 logarithmically spaced bins. The power-law assumption for the spectrum is the same as the one described by van de Kamp et al (Section 2.1, 2016). The ionization rate calculation is based on a continuously-slowing-down approximation and a normalized energy dissipation distribution function for electrons; this method is described in detail by Rees (1989). A prior WACCM simulation was used to provide daily, zonal mean neutral background data for the ionization rate calculation, specifically the concentrations of the main atmospheric constituents N_2 and O_2, and O. The ionization rates were calculated in 3-hour time resolution for each of the L shell bins (latitudes), after the differential electron fluxes were integrated over pitch angles 0-80^o and azimuth angles 0-360^o assuming an isotropic angular distribution. The ionization rates were calculated for the WACCM altitude (km) grid which changes slightly from day to day but corresponds to a fixed pressure level grid. The L shell-dependent ionization rates were then converted to magnetic latitude and, with the assumption of uniformity on magnetic longitude, projected onto the WACCM geographic (latitude-longitude) grid.

Acknowledgments and Data

We are grateful to the three anomymous reviewers for their thorough reviews of this article. The research has been funded by the Norwegian Research Council, through project 222390, "Solar-

Terrestrial Coupling through High Energy Particle Precipitation in the Atmosphere: a Norwegian contribution". YO is also supported by the Norwegian Research Council under contracts 223252/F50. DRM is supported in part by NASA LWS Grant NNX14AH54G. The National Center for Atmospheric Research (NCAR) is sponsored by the U.S. National Science Foundation (NSF). PTV was supported by the Academy of Finland through the project #276926 (SECTIC: Sun-Earth Connection Through Ion Chemistry). DRM, PTV, MAC, and CJR would like to thank the International Space Science Institute, Bern, Switzerland for supporting the project "Quantifying Hemispheric Differences in Particle Forcing Effects on Stratospheric Ozone" (PI: D. R. Marsh). WACCM is a component of the Community Earth System Model (CESM), which is supported by NSF and the Office of Science of the U.S. Department of Energy. WACCM is an open-source community model. All model simulations were performed at NCAR, are archived on the NCAR High Performance Storage System, accessible via the Earth System Grid (https://www.earthsystemgrid.org/), and are also accessible at the Norwegian Center for Research Data (http://www.nsd.uib.no/nsd/english/index.html).

References

Andersson, M. E., P.T. Verronen, D. R. Marsh, S.-M. Paivarinta, and J. M. C. Plane (2016), WACCM-D – Improved modeling of nitric acid and active chlorine during energetic particle precipitation, *J. Geophys. Res.*, doi:10.1002/2015JD024173.

Damiani, A., P. Diego, M. Laurenza, M. Storini, C. Rafanelli (2009), Ozone variability related to several SEP events occurring during solar cycle no. 23, *Advances in Space Research*, 43, 28-40.

Damiani, A., B. Funke, M. López Puertas, M. L. Santee, R. R. Cordero and S. Watanabe (2016), Energetic particle precipitation: A major driver of the ozone budget in the Antarctic upper stratosphere, *Geophys. Res. Lett.*, 43, 3554–3562, doi:10.1002/2016GL068279.

de Zafra, R., and S. P. Smyshlyaev (2001), On the formation of HNO3 in the Antarctic mid to upper stratosphere in winter, *J. Geophys. Res.*, 106, 23, 115–23,125, doi:10.1029/2000JD000314.

Evans, D. S., and M. S. Greer (2004), Polar Orbiting environmental satellite space environment monitor - 2 instrument descriptions and archive data documentation, NOAA technical Memorandum version 1.4, Space Environment Laboratory, Colorado.

Garcia, R. R., M. López-Puertas, B. Funke, D. R. Marsh, D. E. Kinnison, A. K. Smith, and F. González-Galindo (2014), On the distribution of CO2 and CO in the mesosphere and lower thermosphere, *J. Geophys. Res. Atmos.*, 119, doi:10.1002/2013JD021208.

Kawa, S. R., J. B. Kumer, A. R. Douglass, A. E. Roche, S. E. Smith, F. W. Taylor, and D. J. Allen (1995), Missing chemistry of reactive nitrogen in the upper stratospheric polar winter, *Geophys. Res. Lett.*, 22(19), 2629–2632, doi:10.1029/95GL02336.

Kinnison, D. E., et al. (2008), Global observations of HNO3 from the High Resolution Dynamics Limb Sounder (HIRDLS): First results, *J. Geophys. Res.*, 113, D16S44, doi:10.1029/2007JD008814.

Kirkwood, S., A. Osepian, E. Belova, J. Urban, K. Perot, and A. K. Sinha (2015), Ionization and NO production in the polar mesosphere during high-speed solar wind streams: model validation and comparison with NO enhancements observed by Odin-SMR, *Annales Geophysicae*, 33 (5), 561-572, doi:10.5194/angeo-33-561-634-2015.

Kvissel, O.-K., Y. J. Orsolini, F. Stordal, I. S. A. Isaksen, and M. L. Santee (2012), Formation of stratospheric nitric acid by a hydrated ion cluster reaction: Implications for the effect of energetic particle precipitation on the middle atmosphere, *J. Geophys. Res.*, 117, D16301, doi:10.1029/2011JD017257.

Lam, M. M., R. B. Horne, N. P. Meredith, S. A. Glauert, T. Moffat-Griffin, and J. C. Green (2010), Origin of energetic electron precipitation >30 keV into the atmosphere, *J. Geophys. Res.*, 115, A00F08, doi:10.1029/2009JA014619.

López-Puertas, M., B. Funke, S. Gil-López, T. von Clarmann, G. P. Stiller, M. Höpner, S. Kellmann, G. M. Tsidu, H. Fischer, and C. H. Jackman (2005), HNO3, N2O5, and ClONO2 enhancements after the October–November 2003 solar proton events, *J. Geophys. Res.*, 110, A09S44, doi:10.1029/2005JA011051.

Marsh, D. R., R. R. Garcia, D. E. Kinnison, B. A. Boville, F. Sassi, S. C. Solomon, and K. Matthes (2007) Modeling the whole atmosphere response to solar cycle changed in radiative and geomagnetic forcing, *J. Geophys. Res.*, 112, D23306, doi:10.1029/2006JD008306,.

Marsh, D. R. (2011), Chemical–dynamical coupling in the mesosphere and lower thermosphere, in Aeronomy of the Earth's Atmosphere and Ionosphere, IAGA Spec. Sopron Book Ser., vol. 2, pp. 3–17, Springer, Netherlands.

Matthes, K, B. Funke, M. E. Andersson, L. Barnard, J. Beer, P. Charbonneau, M. A. Clilverd, T. Dudok de Wit, M. Haberreiter, A. Hendry, C. H. Jackman, M. Kretzschmar, T. Kruschke, M. Kunze, U. Langematz, D. R. Marsh, A. Maycock, S. Misios, C. J. Rodger, A. A. Scaife, A. Seppälä, M. Shangguan, M. Sinnhuber, K. Tourpali, I. Usoskin, M. van de Kamp, P. T. Verronen, and S. Versick (2017), Solar Forcing for CMIP6 (v3.2), *Geoscientific Model Development*, 10, 2247-2302, doi: 10.5194/gmd-10-2247-2017.

McIlwain, C. E., Coordinates for Mapping the Distribution of Magnetically Trapped Particles (1961), *J. Geophys. Res.*, 66, 3681-3691.

Neal, J. J., C. J. Rodger, and J. C. Green (2013), Empirical determination of solar proton access to the atmosphere: Impact on polar flight paths, *Space Weather*, 11, 420–433, doi:10.1002/swe.20066.

Neal, J. J., C. J. Rodger, M. A. Clilverd, N. R. Thomson, T. Raita, and T. Ulich (2015), Long-term determination of energetic electron precipitation into the atmosphere from AARDDVARK subionospheric VLF observations, *J. Geophys. Res. Space Physics*, 120, 2194–2211, doi:10.1002/ 2014JA020689.

Orsolini, Y. J., G. L. Manney, M. L. Santee, and C. E. Randall (2005), An upper stratospheric layer of enhanced HNO3 following exceptional solar storms, *Geophys. Res. Lett.*, *32*, L12S01, doi:10.1029/2004GL021588.

Orsolini, Y. J., Urban, J., and D.P. Murtagh (2009), Nitric acid in the stratosphere based on Odin observations from 2001 to 2009 – Part 2: High-altitude polar enhancements, *Atmos. Chem. Phys.*, 9, 7045-7052, doi:10.5194/acp-9-7045-2009.

Randall, C. E., V. L. Harvey, C. S. Singleton, S. M. Bailey, P. F. Bernath, M. V. Codrescu, H. Nakajima, and J. M. Russell III (2007), Energetic particle precipitation effects on the Southern Hemisphere stratosphere in 1992-2005, *J. Geophys. Res.*,, 112 (8), doi:10.1029/2006JD007696.

Reddmann, T., et al. (2010), Modelling disturbed stratospheric chemistry during solar-induced NO*x* enhancement observed with MIPAS/ENVISAT, *J. Geophys. Res.*, *115*, D00I11, doi:10.1029/2009JD012569.

Rees, M.H. (1989), Physics and chemistry of the upper atmosphere, Cambridge atmospheric and space science series, Cambridge University Press, Cambridge, UK.

Rienecker, M. M., et al. (2011), MERRA: NASA's modern-era retrospective analysis for research and applications. *J. Clim.*, 24, 3624–3648, doi:10.1175/JCLI-D-11-00015.1.

Rodger, C. J., M. A. Clilverd, J. C. Green, and M. M. Lam (2010a), Use of POES SEM-2 observations to examine radiation belt dynamics and energetic electron precipitation into the atmosphere, *J. Geophys. Res.*, 115, A04202, doi:10.1029/2008JA014023.

Rodger, C. J., B. R. Carson, S. A. Cummer, R. J. Gamble, M. A. Clilverd, J. C. Green, J.-A. Sauvaud, M. Parrot, and J.-J. Berthelier (2010b), Contrasting the efficiency of radiation belt losses caused by ducted and nonducted whistler-mode waves from ground-based transmitters, *J. Geophys. Res.*, 115, A12208, doi:10.1029/2010JA015880.

Rodger, C. J., A. J. Kavanagh, M. A. Clilverd, and S. R. Marple (2013), Comparison between POES energetic electron precipitation observations and riometer absorptions: Implications for determining true precipitation fluxes, *J. Geophys. Res. Space Physics*, 118, 7810–7821, doi:10.1002/2013JA019439.

Santee, M. L., G. L. Manney, N. J. Livesey, and W. G. Read (2004), Three dimensional structure and evolution of stratospheric HNO3 based on UARS Microwave Limb Sounder measurements, *J. Geophys. Res.*, 109, D15306, doi:10.1029/2004JD004578.

Sinnhuber, M., H. Nieder, and N. Wieters (2012), Energetic Particle Precipitation and the Chemistry of the Mesosphere/Lower Thermosphere, *Surv. Geophys.*, 33, 1281–1334.

Smith, A. K., M. López-Puertas, B. Funke, M. García-Comas, M. G. Mlynczak, and L. A. Holt (2015), Nighttime ozone variability in the high latitude winter mesosphere, *J. Geophys. Res. Atmos.*, 119, 13,547–13,564, doi:10.1002/2014JD021987.

Smith-Johnsen, C., H. Nesse Tyssøy, K. Hendrickx, Y. Orsolini, G. Kishore Kumar, L.-K. G. Ødegaard, M. I. Sandanger, F. Stordal, and L. Megner (2017), Direct and indirect electron precipitation effect on nitric oxide in the polar middle atmosphere, using a full-range energy spectrum, *J. Geophys. Res. Space Physics*, 122, 8679–8693, doi:10.1002/2017JA024364.

Stiller, G. P., et al. (2005), An enhanced HNO3 second maximum in the Antarctic midwinter upper stratosphere in 2003, *J. Geophys. Res.,* 110, D20303, doi:10.1029/2005JD006011.

Turunen, E., A. Kero, P. T. Verronen, Y. Miyoshi, S.-I. Oyama, and S. Saito (2016), Mesospheric ozone destruction by high-energy electron precipitation associated with pulsating aurora, J. Geophys. Res. Atmos., 121, 11,852–11,861, doi:10.1002/2016JD025015.

Urban, J., M. Pommier, D. P. Murtagh, M. L. Santee, and Y. J. Orsolini (2009), Nitric acid in the stratosphere based on Odin observations from 2001 to 2009–Part 1: A global climatology, *Atmos. Chem. Phys.*, 9, 7031–7044, doi:10.5194/acp-9-7031-2009.

van de Kamp, M., A. Seppälä, M.A. Clilverd, C.J. Rodger, P.T. Verronen, and I.C. Whittaker (2016), A model providing long-term datasets of energetic electron precipitation during geomagnetic storms, *J. Geophys. Res.*, 121, 12520-12540. DOI: 10.1002/2015JD024212.

Verronen, P. T., et al. (2008), About the increase of HNO3 in the stratopause region during the Halloween 2003 solar proton event, *Geophys. Res. Lett.*, *35*, L20809, doi:10.1029/2008GL035312.

Verronen, P. T., et al. (2011), Nitric acid enhancements in the mesosphere during the January 2005 and December 2006 solar proton events, *J. Geophys. Res.*, 116, D17301, doi:10.1029/2011JD016075.

Verronen, P. T. and R. Lehmann (2013), Analysis and parameterisation of ionic reactions affecting middle atmospheric HOx and NOy during solar proton events, *Annales Geophysicae*, 31, 909–956, doi:10.5194/angeo-31-909-2013.

Verronen, P. T., M. E. Andersson, D. R. Marsh, T. Kovacs, and J. M. C. Plane (2016), WACCM-D – Whole Atmosphere Community Climate Model with D-region ion chemistry, *J. Adv. Model Earth Syst.*, 8, 954–975, doi:10.1002/2015MS000592.

Whittaker, I. C., R. J. Gamble, C. J. Rodger, M. A. Clilverd, and J.-A. Sauvaud (2013), Determining the spectra of radiation belt electron losses: Fitting DEMETER electron flux observations for typical and storm times, *J. Geophys. Res. Space Physics*, 118, 7611–7623, doi:10.1002/2013JA019228.

Whittaker, I. C., C. J. Rodger, M. A. Clilverd, and J.-A. Sauvaud (2014), The effects and correction of the geometric factor for the POES/MEPED electron flux instrument using a multisatellite comparison, *J. Geophys. Res. Space Physics*, 119, doi:10.1002/2014JA020021.

714 Yando, K., R. M. Millan, J. C. Green, and D. S. Evans (2011), A Monte Carlo simulation of the
715 NOAA POES Medium Energy Proton and Electron Detector instrument, *J. Geophys. Res.*, 116,
716 A10231, doi:10.1029/2011JA016671
717

Captions

FIGURE 1: **Monthly-mean polar cap average of HNO_3 (in ppb, log10 scale).** Period is from July 2009 until June 2010, for both the southern hemisphere (a,c,e, over latitudes poleward of 50°S) and northern hemisphere (b,d,f, over latitudes poleward of 50°N), from 40 to 110 km. (a,b) standard WACCM, (c,d) WACCM-D, and (e,f) the ratio (WACCM-D / WACCM), also in log scale. All simulations are with MEEs included.

FIGURE 2: **Time evolution of HNO_3 (in ppb)**. (left) Monthly-mean annual (July 2009-June 2010) evolution of HNO_3 in WACCM-D with MEE included, for the southern hemisphere (black dashed line, over latitudes poleward of 50°S) and the northern hemisphere (black solid line, over latitudes poleward of 50°N) averaged over the 70-75 km layer. Corresponding results form simulations without MEEs are also shown (red lines). (right) Same but showing daily evolution in April and May 2010 for simulations with MEEs included.

FIGURE 3: **Winter-averaged vertical profiles of the three neutral species (in ppb, log10 scale).** Shown are the three neutral species HNO_3, NO_3 and N_2O_5 in WACCM (dashed lines) and WACCM-D (solid lines) in JJA for the southern hemisphere (left column, latitudes poleward of 50°S), and in DJF for the northern hemisphere (right column, latitudes poleward of 50°N). All simulations are with MEEs included.

FIGURE 4: **Monthly-mean polar cap average of key ion clusters (in ppb, log10 scale).** (a,b) $NO_3^-(H_2O)_n$, (c,d) $H^+(H_2O)_n$, (e,f) $NO^+(H_2O)_n$ and (g,h) $NO_3^-(HNO_3)_n$ from July 2009 until June 2010, for both the southern hemisphere (a,c,e,g, over latitudes poleward of 50°S) and northern hemisphere (b,d,f,h, over latitudes poleward of 50°N) in WACCM-D. The two white lines are the contours of 2 and 5 ppm of H_2O (upper and lower contours, respectively). All simulations are with MEEs included.

FIGURE 5: **Daily-mean polar cap average of HNO_3 (in ppb, log10 scale)**. The period is April-May 2010, for both the southern hemisphere (a,c,e, over latitudes poleward of 50°S) and northern hemisphere (b,d,f, over latitudes poleward of 50°N) from 40 to 110 km. (a,b) standard WACCM, (c,d) WACCM-D, and (e,f) the ratio (WACCM-D / WACCM), also in log scale. (g,h) the Dst-index for the same period to highlight the timing of geomagnetic activity. All simulations are with MEEs included.

FIGURE 6: **Daily-mean polar cap average of key ion clusters (in ppb, log10 scale).** (a,b) $NO_3^-(H_2O)_n$, (c,d) $H^+(H_2O)_n$, (e,f) $NO^+(H_2O)_n$ and (g,h) $NO_3^-(HNO_3)_n$ for April-May 2010, for both the southern hemisphere (a,c,e,g, over latitudes poleward of 50°S) and northern hemisphere (b,d,f,h, over latitudes poleward of 50°N) in WACCM-D. (i,j) the Dst-index for the same period to highlight the timing of geomagnetic activity. The two white lines are the contours of 2 and 5 ppm of H_2O. All simulations are with MEEs included.

FIGURE 7: **Vertical profiles of abundance of ion clusters and neutral species (in ppb, log10 scale).** Three-day averages in quiet conditions (April 1-3, dashed lines) and active conditions (April 6-8, solid lines) (southern hemisphere in left column, latitudes poleward of 50°S, and northern hemisphere in right column, latitudes poleward of 50°N) of the vertical profiles of

764 abundance of the four key ion clusters and the neutral species HNO_3, NO_3 and N_2O_5 in
765 WACCM-D. All simulations are with MEEs included.
766
767 FIGURE 8: **Geographic maps of HNO_3 (in ppb, log10 scale) over the northern hemisphere**.
768 Maps correspond to 3-day averages at 70 km, in quiet (left column for April 1-3) and active
769 (middle column for April 6-8) conditions. Upper row shows the standard WACCM, second row
770 shows WACCM-D. In this figure and all following figures with maps, latitude circles are at 45°,
771 60° and 75°, and zero degree longitude is at the bottom. All simulations are with MEEs included.
772
773 FIGURE 9: **Geographic maps of HNO_3 (in ppb, log10 scale) over the southern hemisphere.**
774 (As in Fig. 8)
775
776 FIGURE 10: **Geographic maps of key ion clusters (in ppb) over the northern hemisphere.**
777 Shown are $NO_3^-(H_2O)_n$, $H^+(H_2O)_n$, $NO^+(H_2O)_n$ and $NO_3^-(HNO_3)_n$ from WACCM-D at 70 km,
778 in quiet (left column for April 1-3) and active (right column for April 6-8) conditions. All
779 simulations are with MEEs included.
780
781 FIGURE 11: **Geographic maps of key ion clusters (in ppb) over the southern hemisphere.**
782 (As in Fig. 10).
783
784 FIGURE 12: **April-mean latitude/height zonal-mean cross-sections of HNO_3 (in ppb, log10**
785 **scale) for all simulations**. (a,b,c) standard WACCM without and with MEE and their absolute
786 difference (the later minus the former), respectively. (d,e,f) standard WACCM without and with
787 MEE and their absolute difference(the later minus the former), respectively. (g,h) absolute
788 difference between WACCM-D and WACCM without and with MEE. (i) absolute difference
789 beween WACCM-D with MEE and WACCM without MEE. Difference are expressed in ppb.
790
791 FIGURE 13: **Vertical profiles of abundance of ion clusters (in ppb, log10 scale) in**
792 **simulations with and without MEEs**. Profiles of the four key ion clusters in WACCM-D
793 correspond to 3-day averages during the active period (April 6-8) for southern hemisphere (left,
794 latitudes poleward of 50°S) and northern hemisphere (right, latitudes poleward of 50°N), with
795 MEEs included (solid lines) and without (dashed lines). Colour coding for the ion clusters is the
796 same as in Fig. 7.
797
798

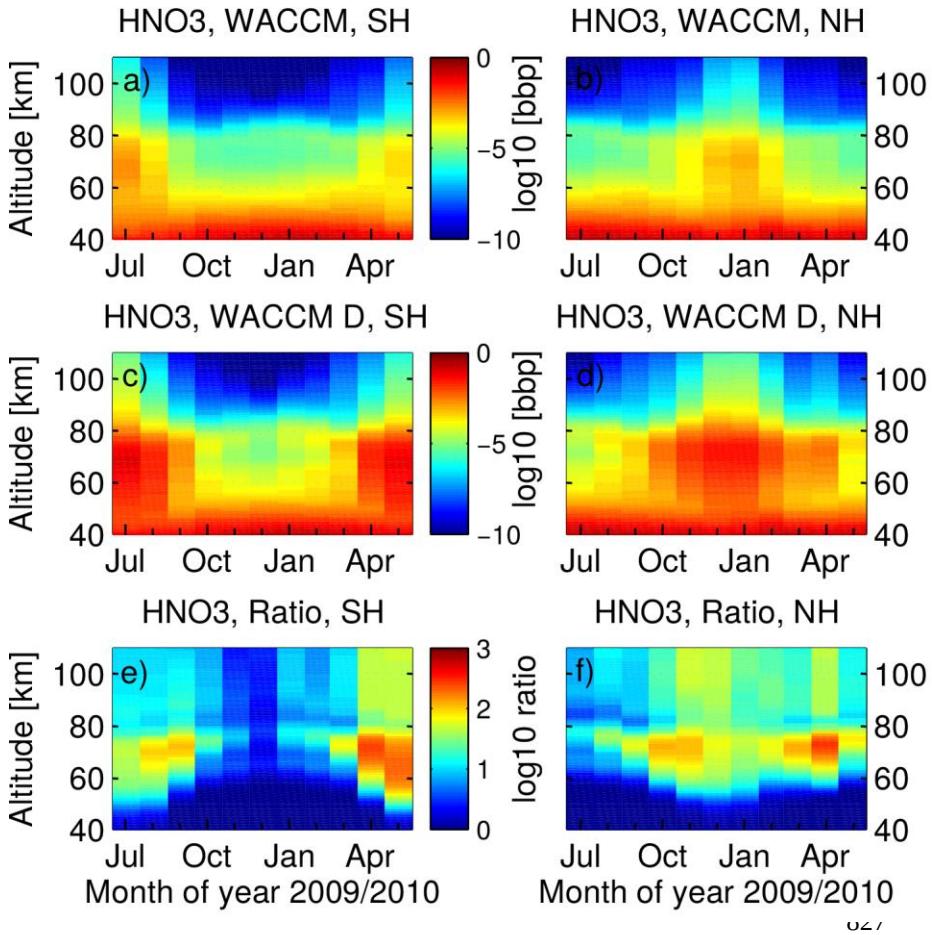

FIGURE 1: **Monthly-mean polar cap average of HNO_3 (in ppb, log10 scale).** Period is from July 2009 until June 2010, for both the southern hemisphere (a,c,e, over latitudes poleward of 50°S) and northern hemisphere (b,d,f, over latitudes poleward of 50°N), from 40 to 110 km. (a,b) standard WACCM, (c,d) WACCM-D, and (e,f) the ratio (WACCM-D / WACCM), also in log scale. All simulations are with MEEs included.

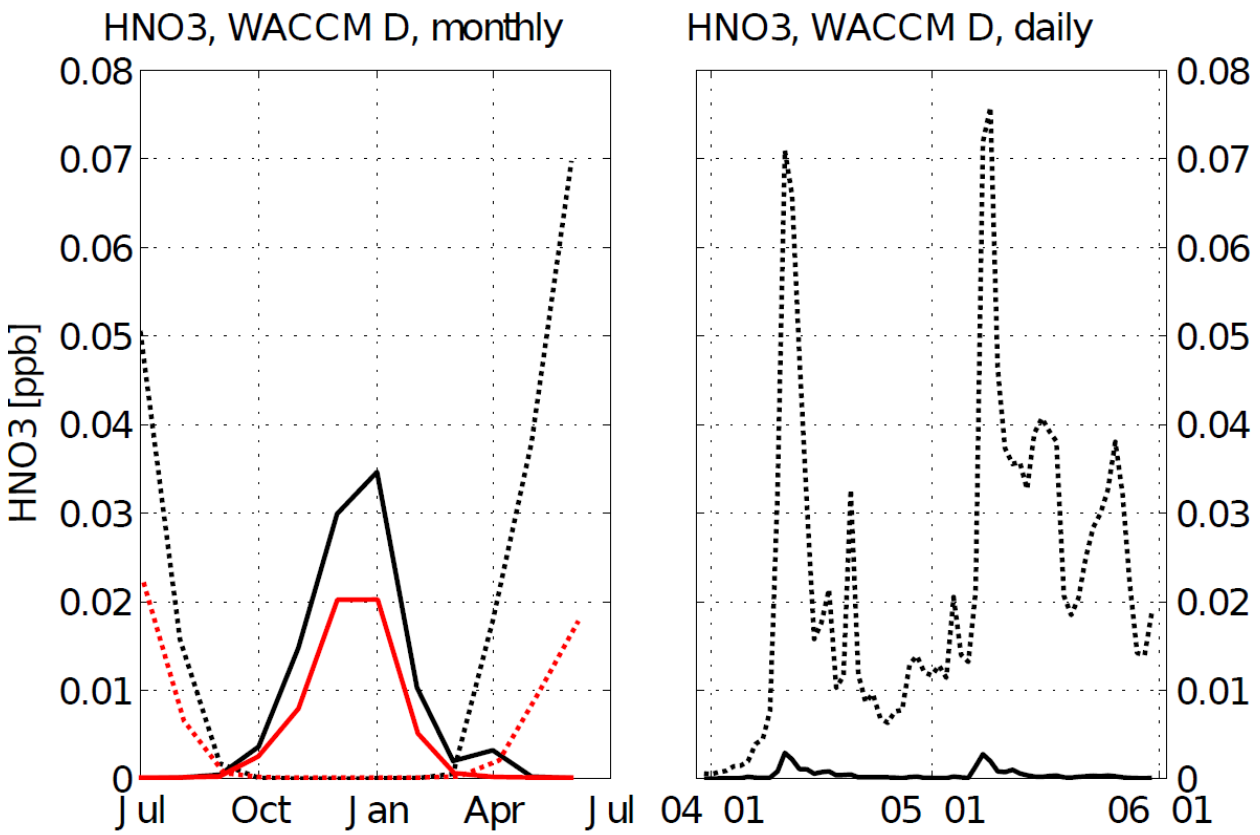

FIGURE 2: **Time evolution of HNO_3 (in ppb)**. (left) Monthly-mean annual (July 2009-June 2010) evolution of HNO_3 in WACCM-D with MEE included, for the southern hemisphere (black dashed line, over latitudes poleward of 50°S) and the northern hemisphere (black solid line, over latitudes poleward of 50°N) averaged over the 70-75 km layer. Corresponding results from simulations without MEEs are also shown (red lines). (right) Same but showing daily evolution in April and May 2010 for simulations with MEEs included.

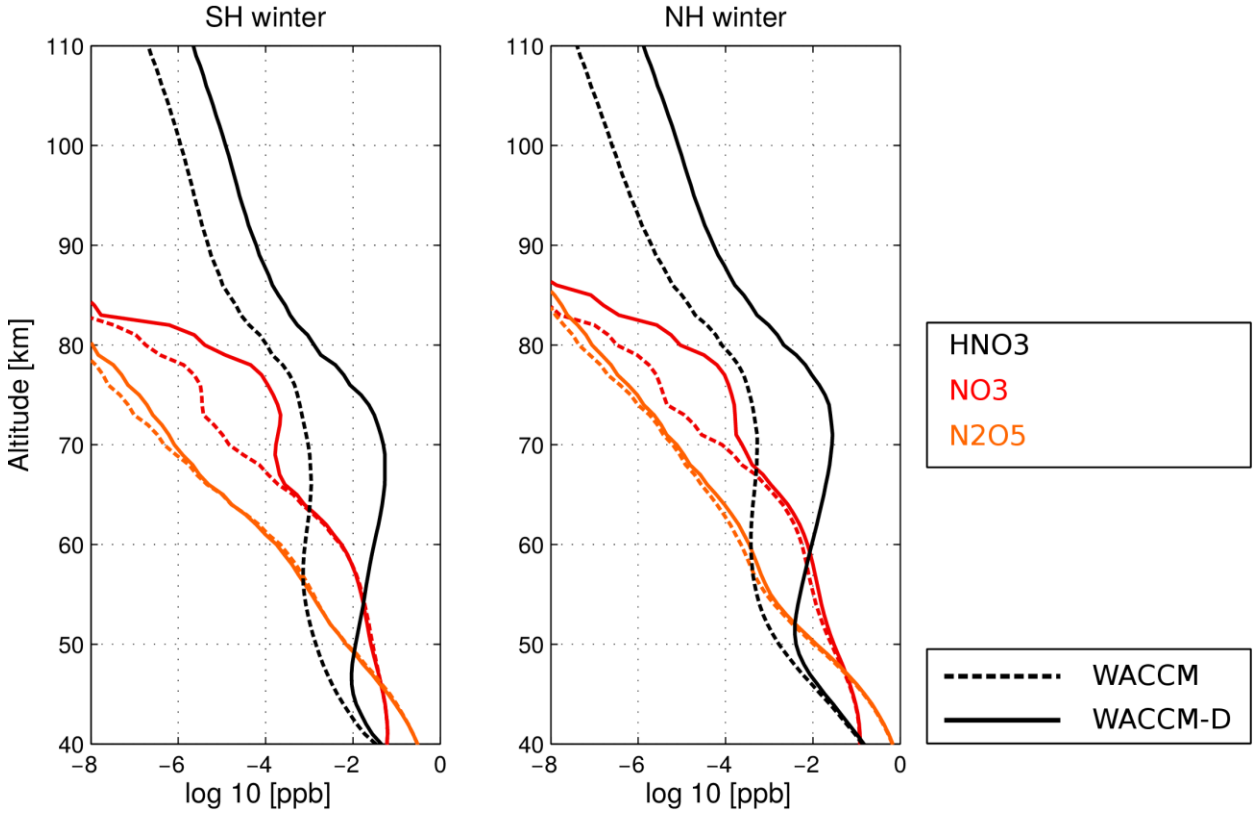

FIGURE 3: **Winter-averaged vertical profiles of the three neutral species (in ppb, log10 scale).** Shown are the three neutral species HNO_3, NO_3 and N_2O_5 in WACCM (dashed lines) and WACCM-D (solid lines) in JJA for the southern hemisphere (left column, latitudes poleward of 50°S), and in DJF for the northern hemisphere (right column, latitudes poleward of 50°N). All simulations are with MEEs included.

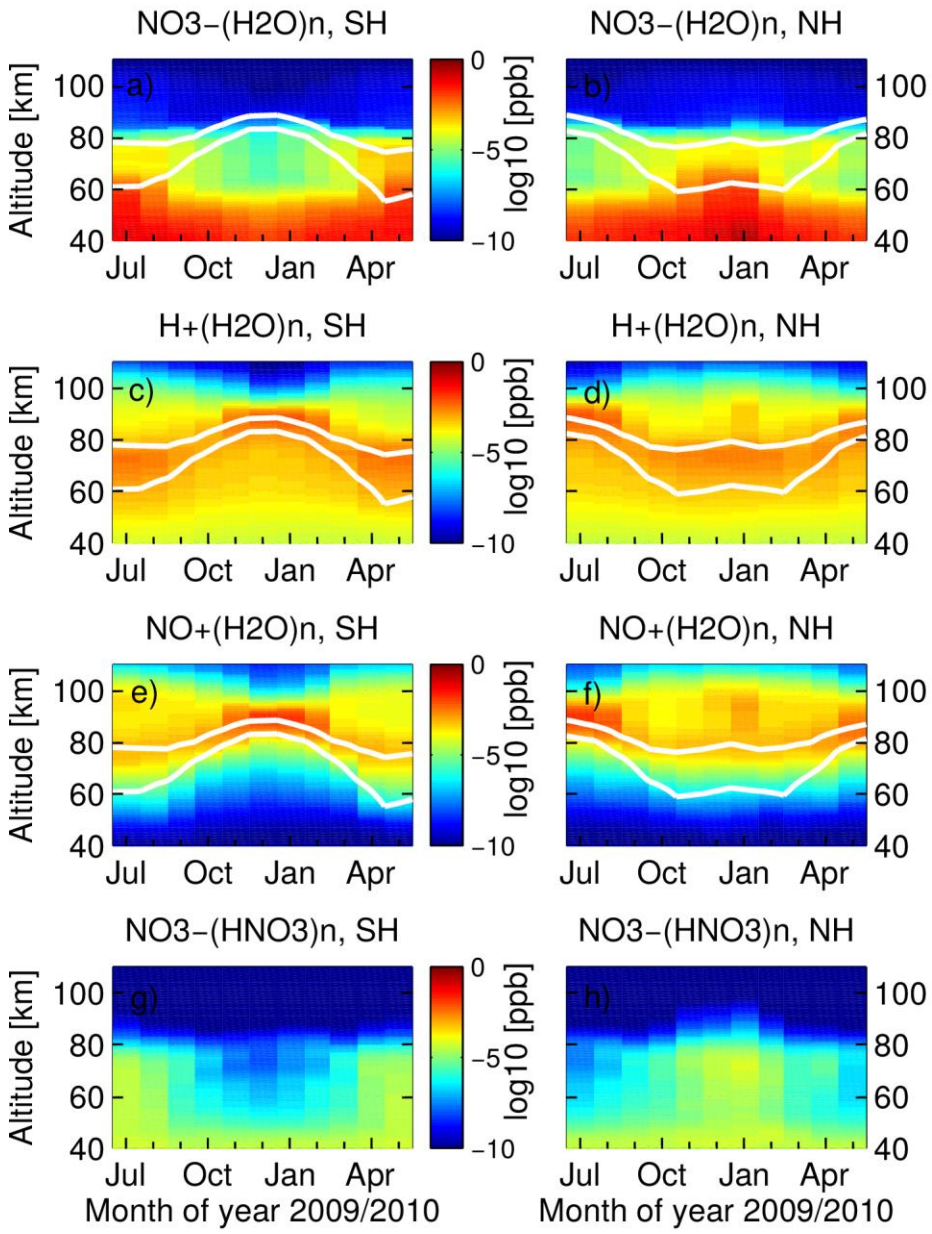

FIGURE 4: **Monthly-mean polar cap average of key ion clusters (in ppb, log10 scale).** (a,b) $NO_3^-(H_2O)_n$, (c,d) $H^+(H_2O)_n$, (e,f) $NO^+(H_2O)_n$ and (g,h) $NO_3^-(HNO_3)_n$ from July 2009 until June 2010, for both the southern hemisphere (a,c,e,g, over latitudes poleward of 50°S) and northern hemisphere (b,d,f,h, over latitudes poleward of 50°N) in WACCM-D. The two white lines are the contours of 2 and 5 ppm of H_2O (upper and lower contours, respectively). All simulations are with MEEs included.

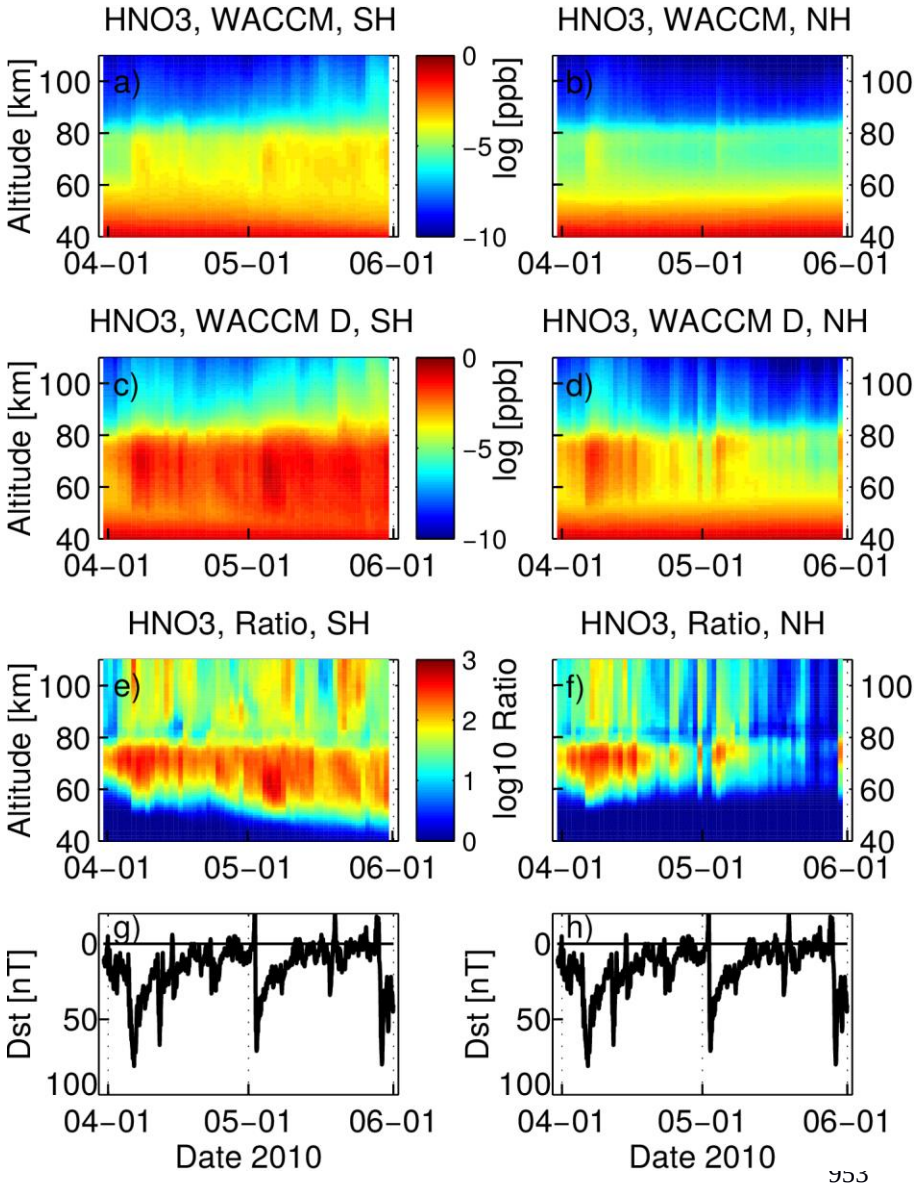

FIGURE 5: **Daily-mean polar cap average of HNO_3 (in ppb, log10 scale)**. The period is April-May 2010, for both the southern hemisphere (a,c,e, over latitudes poleward of 50°S) and northern hemisphere (b,d,f, over latitudes poleward of 50°N) from 40 to 110 km. (a,b) standard WACCM, (c,d) WACCM-D, and (e,f) the ratio (WACCM-D / WACCM), also in log scale. (g,h) the Dst-index for the same period to highlight the timing of geomagnetic activity. All simulations are with MEEs included.

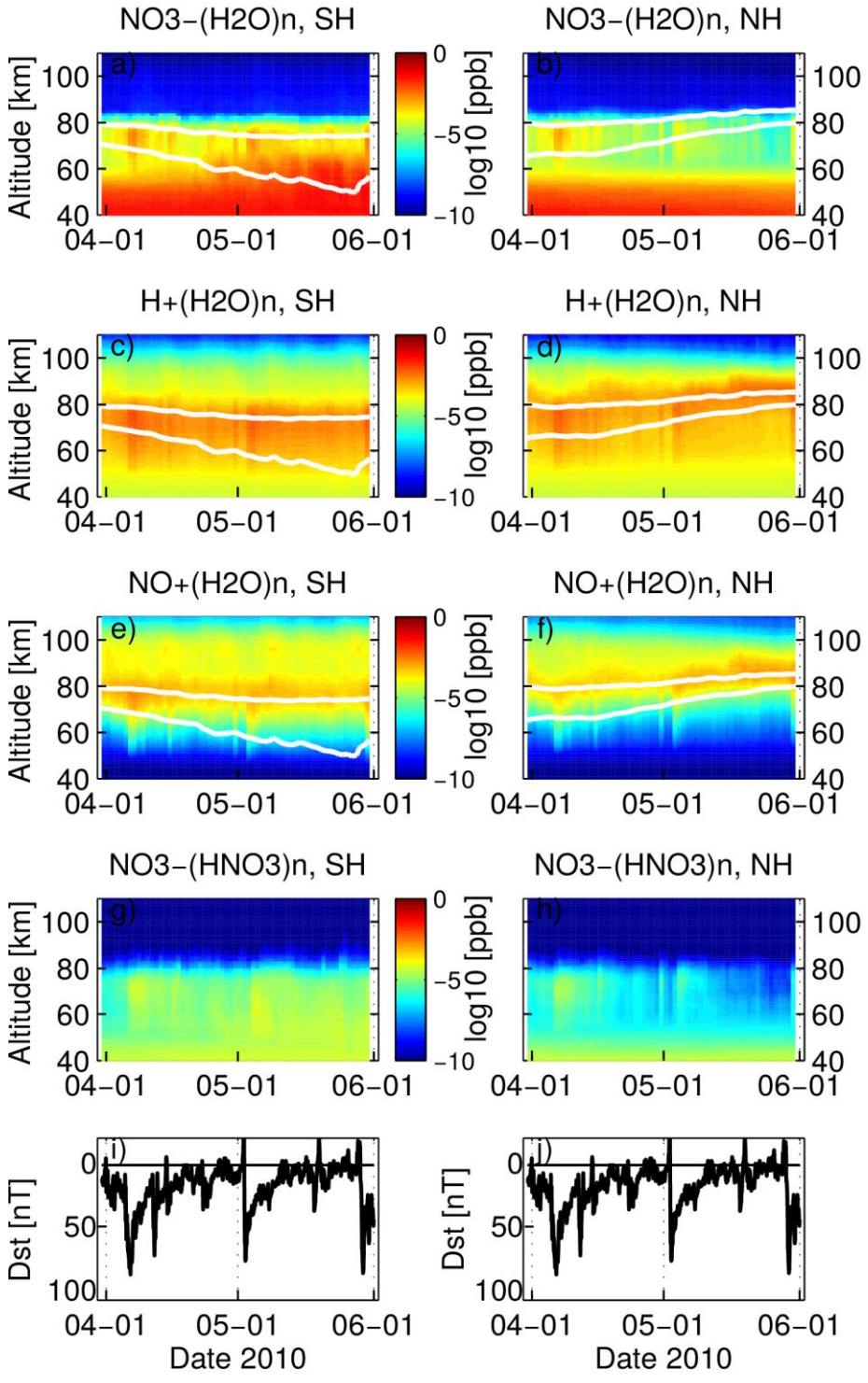

1006

1007 FIGURE 6:**Daily-mean polar cap average of key ion clusters (in ppb, log10 scale).** (a,b) NO_3^-
1008 $(H_2O)_n$, (c,d) $H^+(H_2O)_n$, (e,f) $NO^+(H_2O)_n$ and (g,h) $NO_3^-(HNO_3)_n$ for April-May 2010, for both
1009 the southern hemisphere (a,c,e,g, over latitudes poleward of 50°S) and northern hemisphere
1010 (b,d,f,h, over latitudes poleward of 50°N) in WACCM-D. (i,j) the Dst-index for the same period

1011 to highlight the timing of geomagnetic activity. The two white lines are the contours of 2 and 5
1012 ppm of H_2O. All simulations are with MEEs included.
1013
1014

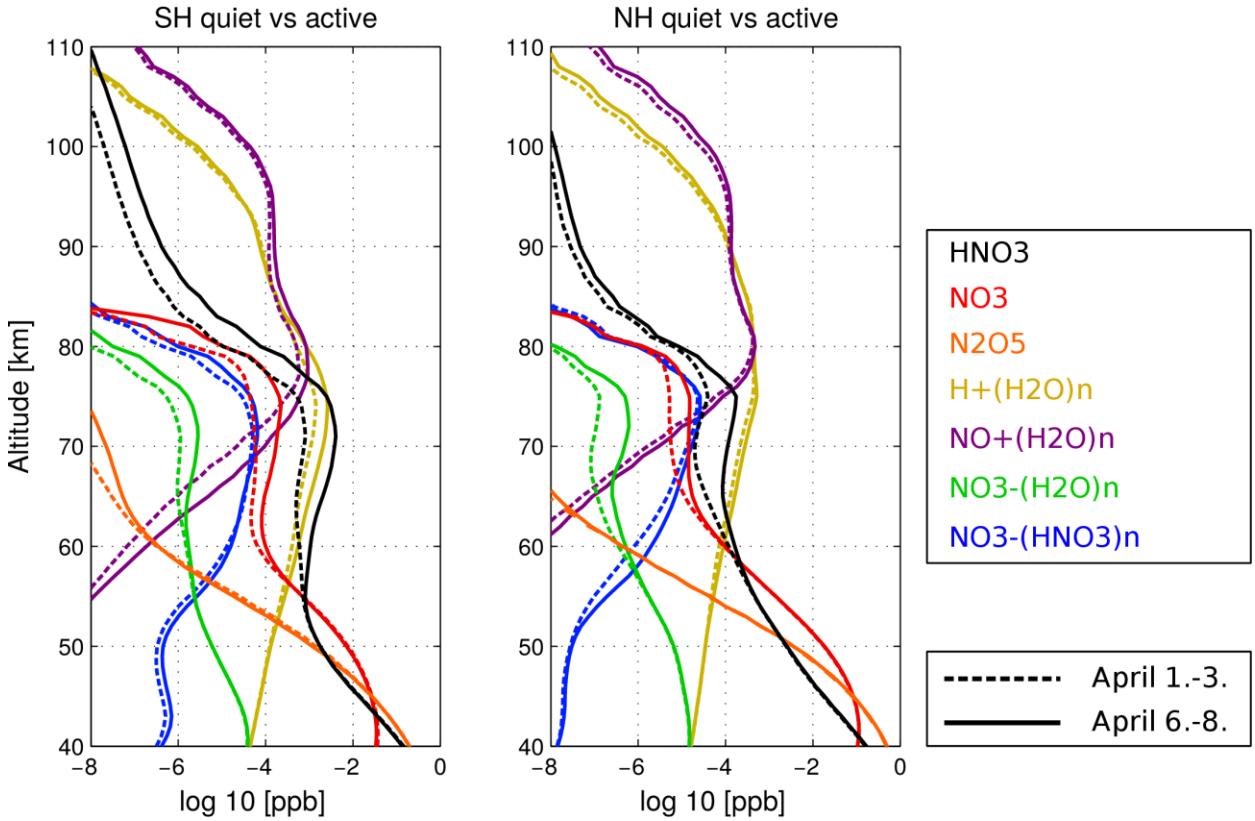

FIGURE 7: **Vertical profiles of abundance of ion clusters and neutral species (in ppb, log10 scale).** Three-day averages in quiet conditions (April 1-3, dashed lines) and active conditions (April 6-8, solid lines) (southern hemisphere in left column, latitudes poleward of 50°S, and northern hemisphere in right column, latitudes poleward of 50°N) of the vertical profiles of abundance of the four key ion clusters and the neutral species HNO_3, NO_3 and N_2O_5 in WACCM-D. All simulations are with MEEs included.

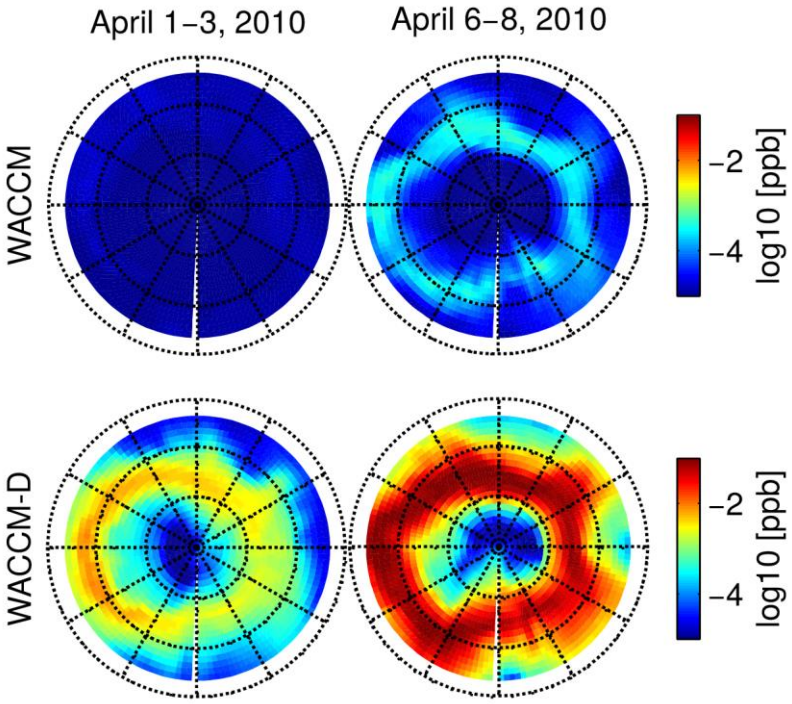

FIGURE 8: **Geographic maps of HNO_3 (in ppb, log10 scale) over the northern hemisphere**. Maps correspond to 3-day averages at 70 km, in quiet (left column for April 1-3) and active (middle column for April 6-8) conditions. Upper row shows the standard WACCM, second row shows WACCM-D. In this figure and all following figures with maps, latitude circles are at 45°, 60° and 75°, and zero degree longitude is at the bottom. All simulations are with MEEs included.

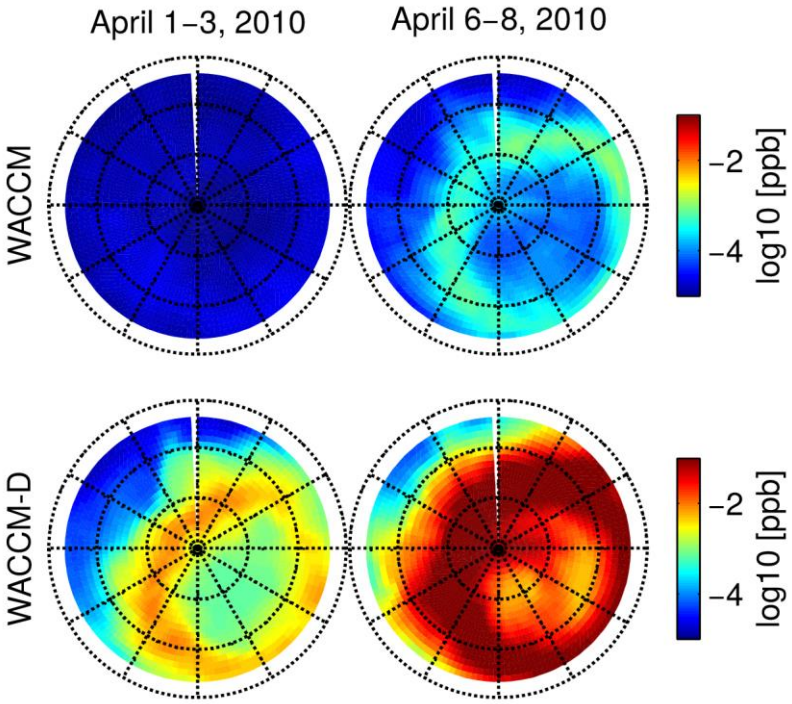

FIGURE 9: **Geographic maps of HNO_3 (in ppb, log10 scale) over the southern hemisphere.** (As in Fig. 8)

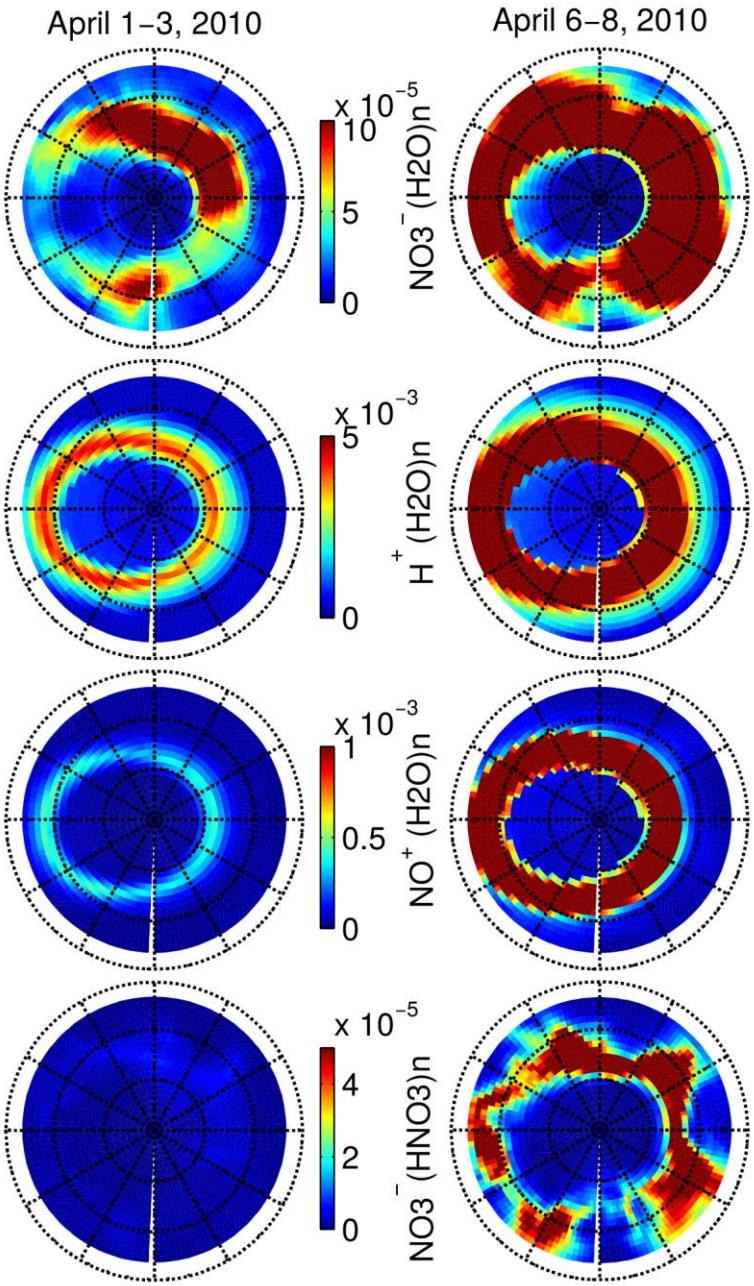

FIGURE 10: **Geographic maps of key ion clusters (in ppb) over the northern hemisphere.** Shown are $NO_3^-(H_2O)_n$, $H^+(H_2O)_n$, $NO^+(H_2O)_n$ and $NO_3^-(HNO_3)_n$ from WACCM-D at 70 km, in quiet (left column for April 1-3) and active (right column for April 6-8) conditions. All simulations are with MEEs included.

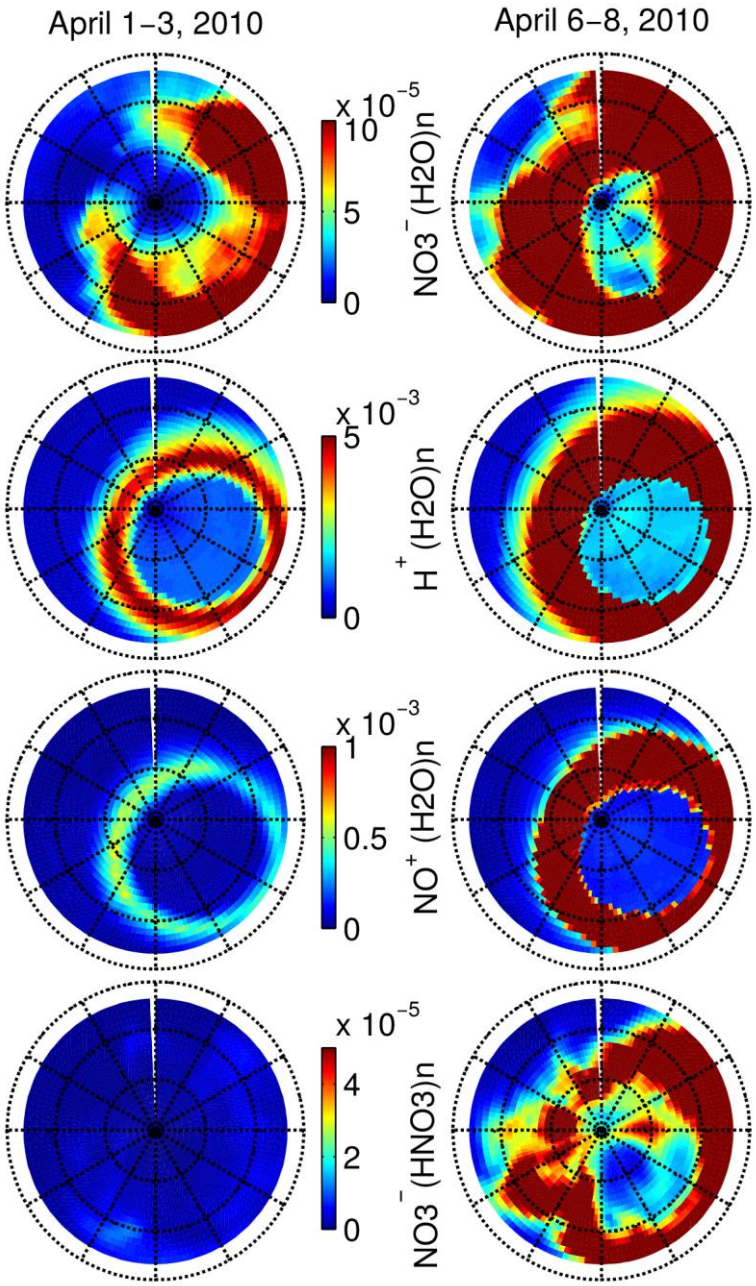

FIGURE 11: **Geographic maps of key ion clusters (in ppb) over the southern hemisphere.** (As in Fig. 10).

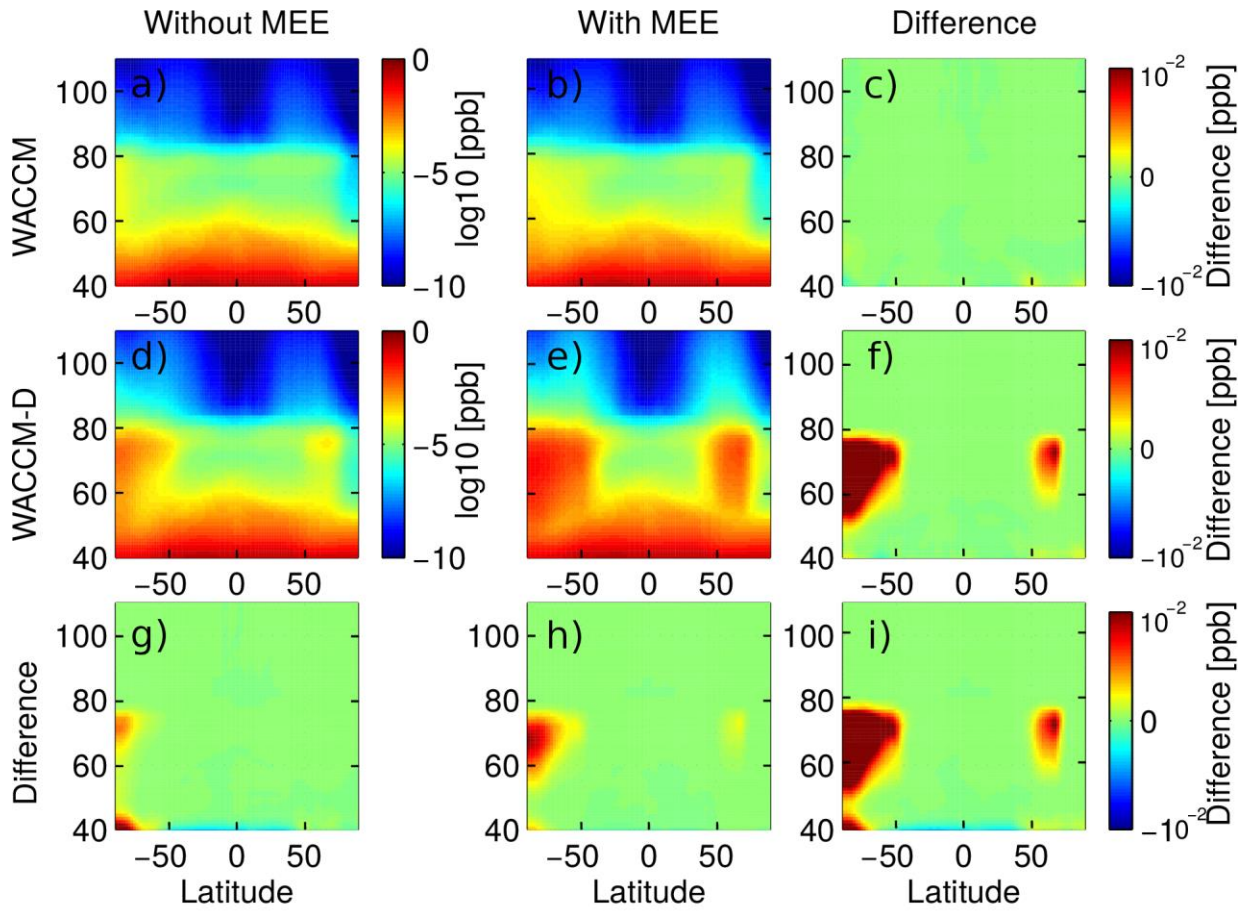

FIGURE 12: **April-mean latitude/height zonal-mean cross-sections of HNO_3 (in ppb, log10 scale) for all simulations**. (a,b,c) standard WACCM without and with MEE and their absolute difference (the latter minus the former), respectively. (d,e,f) WACCM-D without and with MEE and their absolute difference(the latter minus the former), respectively. (g,h) absolute difference between WACCM-D and standard WACCM without and with MEE. (i) absolute difference between WACCM-D with MEE and standard WACCM without MEE. Difference are expressed in ppb.

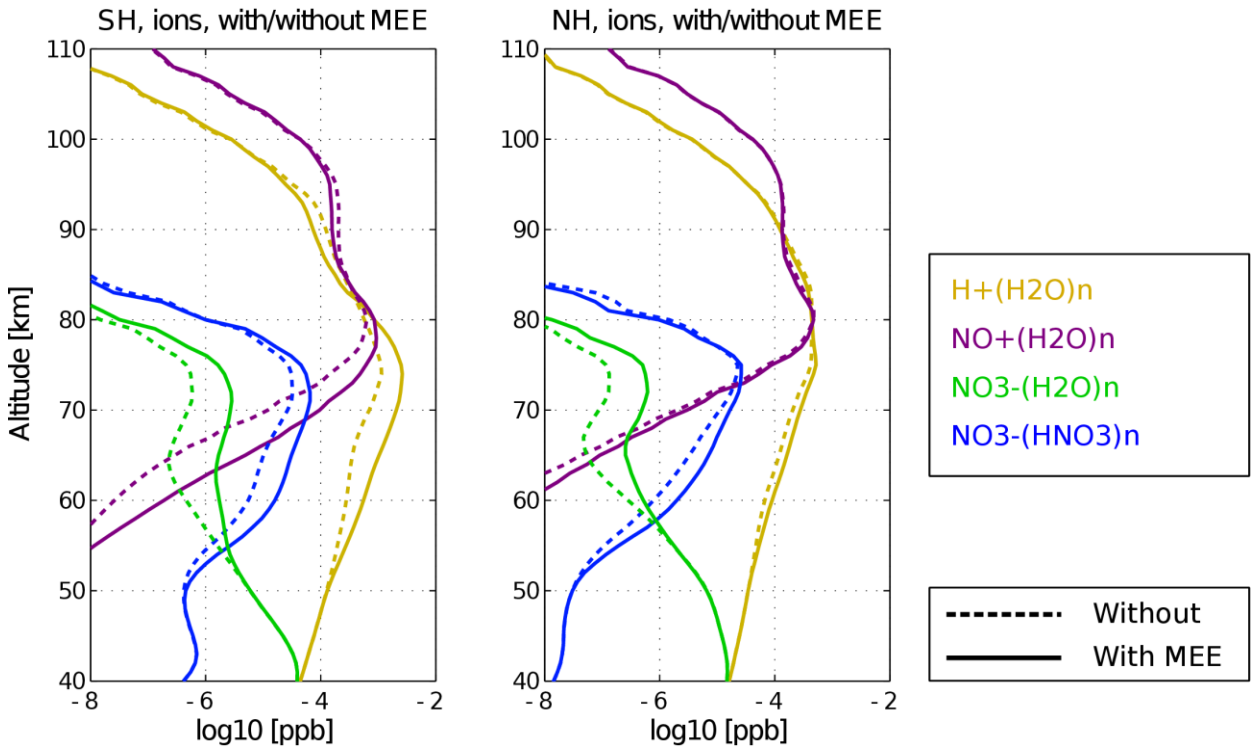

FIGURE 13: **Vertical profiles of abundance of ion clusters (in ppb, log10 scale) in simulations with and without MEEs**. Profiles of the four key ion clusters in WACCM-D correspond to 3-day averages during the active period (April 6-8) for southern hemisphere (left, latitudes poleward of 50°S) and northern hemisphere (right, latitudes poleward of 50°N), with MEEs included (solid lines) and without (dashed lines). Colour coding for the ion clusters is the same as in Fig. 7.

Figure 1.

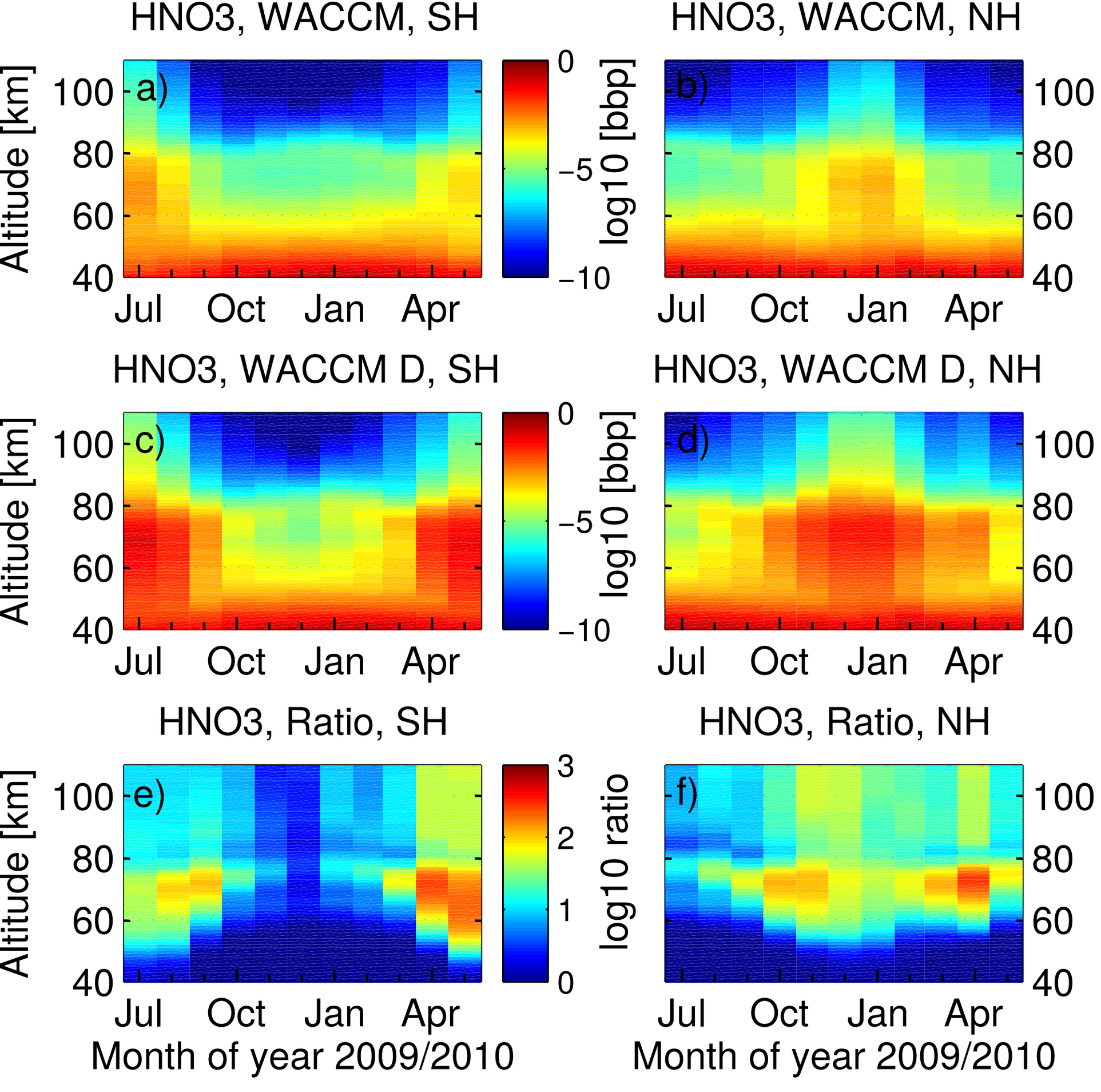
HNO3, WACCM, SH
HNO3, WACCM, NH
HNO3, WACCM D, SH
HNO3, WACCM D, NH
HNO3, Ratio, SH
HNO3, Ratio, NH
a)
b)
c)
d)
e)
f)
Altitude [km]
100
80
60
40
Jul
Oct
Jan
Apr
0
−5
−10
log10 [bbp]
3
2
1
0
log10 ratio
Month of year 2009/2010

Figure 2.

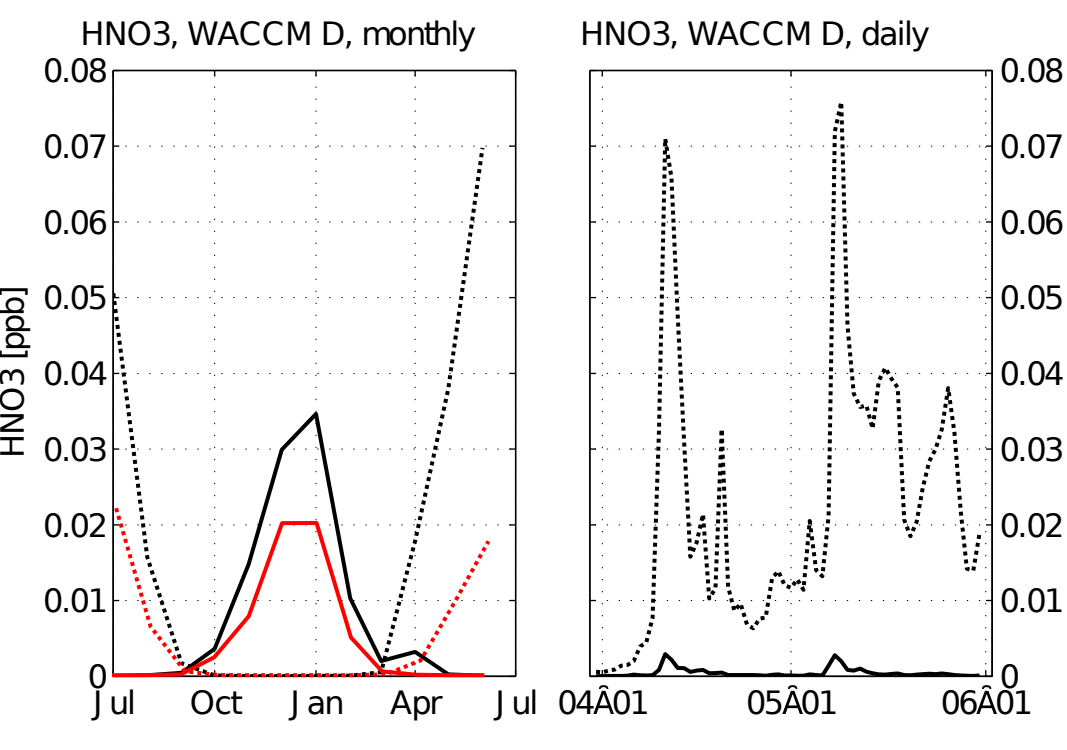
HNO3, WACCM D, monthly
HNO3, WACCM D, daily
HNO3 [ppb]
0.08
0.07
0.06
0.05
0.04
0.03
0.02
0.01
0
Jul
Oct
Jan
Apr
Jul
04Â01
05Â01
06Â01

Figure 3.

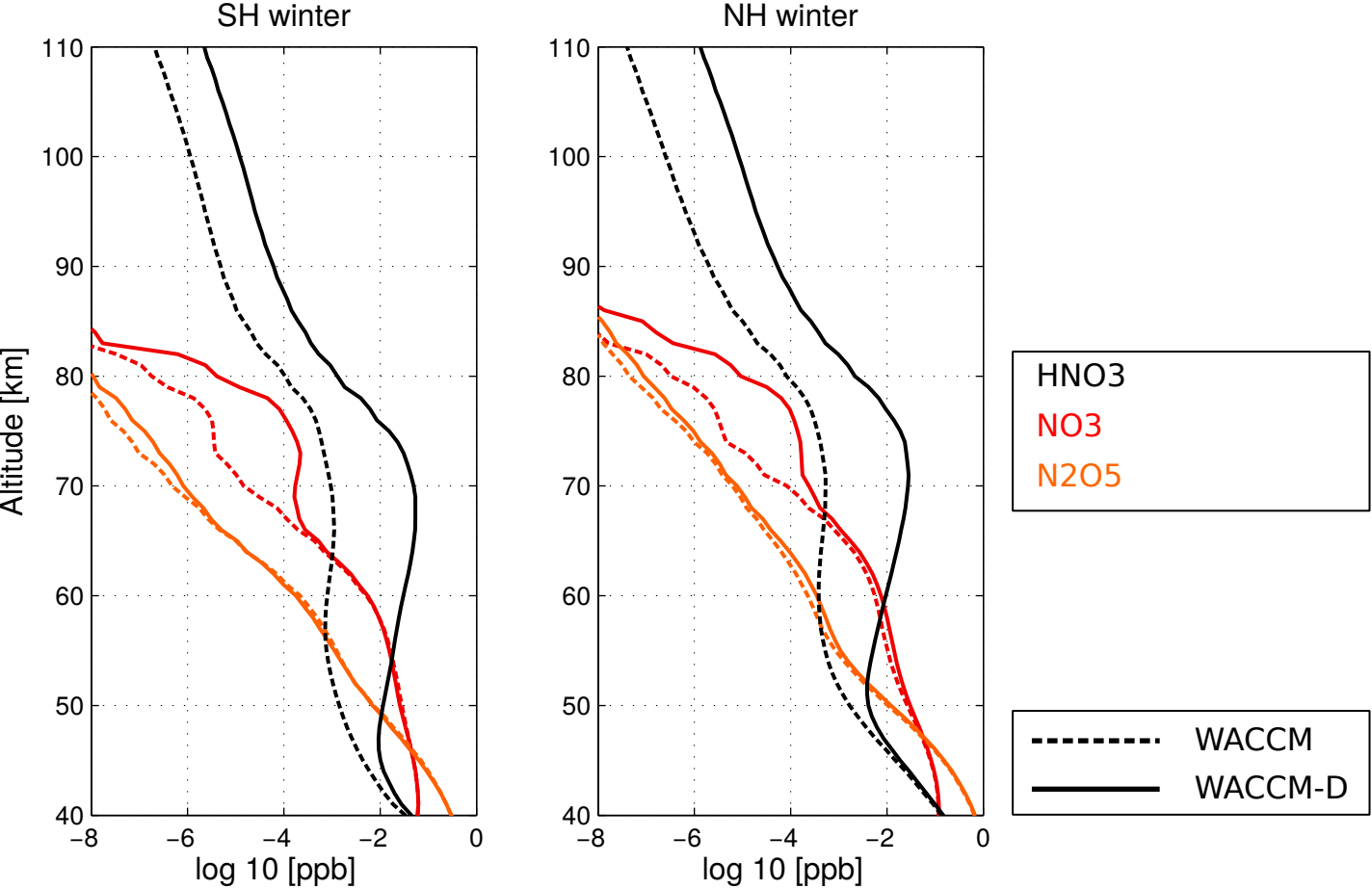
SH winter
NH winter
Altitude [km]
110
100
90
80
70
60
50
40
−8
−6
−4
−2
0
log 10 [ppb]
HNO3
NO3
N2O5
WACCM
WACCM-D

Figure 4.

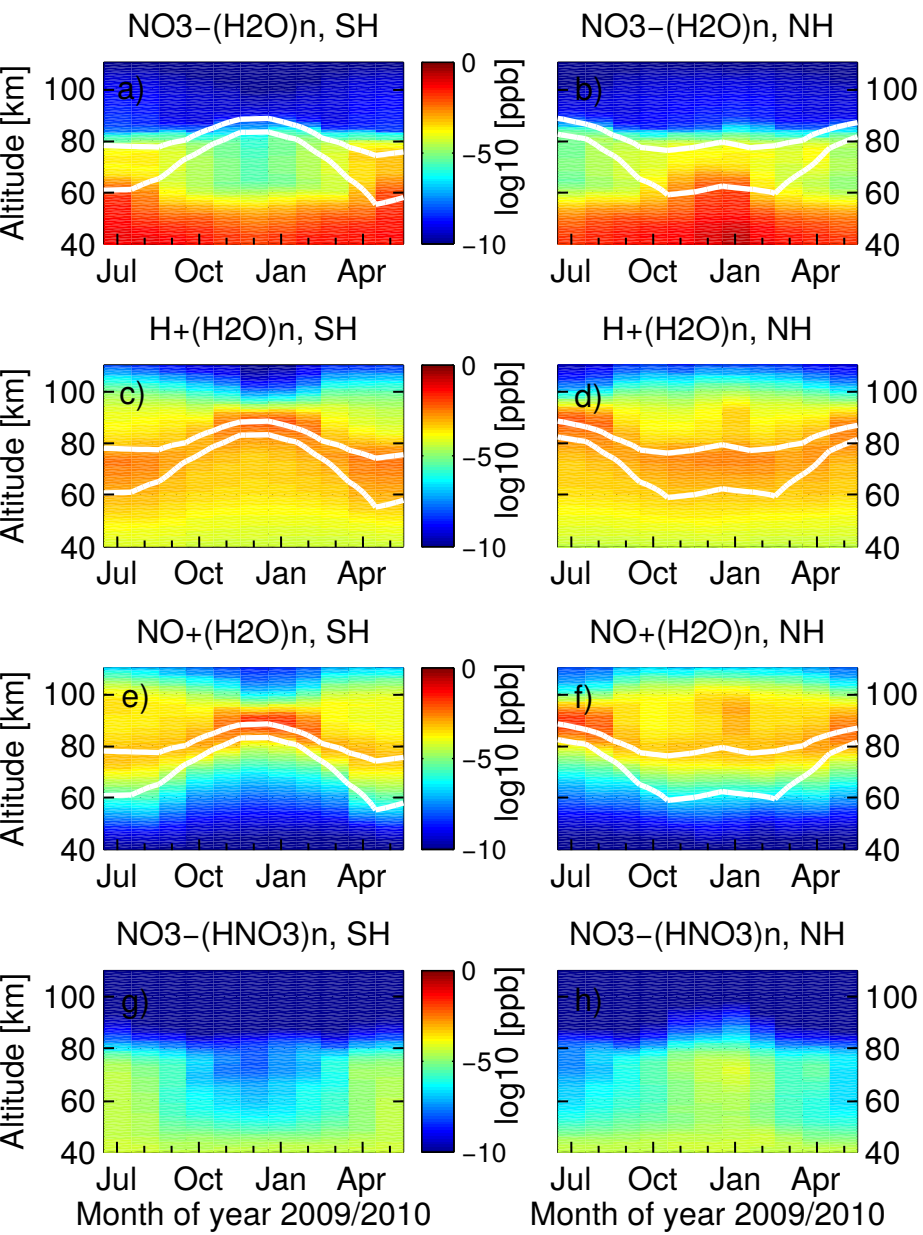
NO3−(H2O)n, SH
NO3−(H2O)n, NH
H+(H2O)n, SH
H+(H2O)n, NH
NO+(H2O)n, SH
NO+(H2O)n, NH
NO3−(HNO3)n, SH
NO3−(HNO3)n, NH
a)
b)
c)
d)
e)
f)
g)
h)
Altitude [km]
100
80
60
40
Jul
Oct
Jan
Apr
0
−5
−10
log10 [ppb]
Month of year 2009/2010

Figure 5.

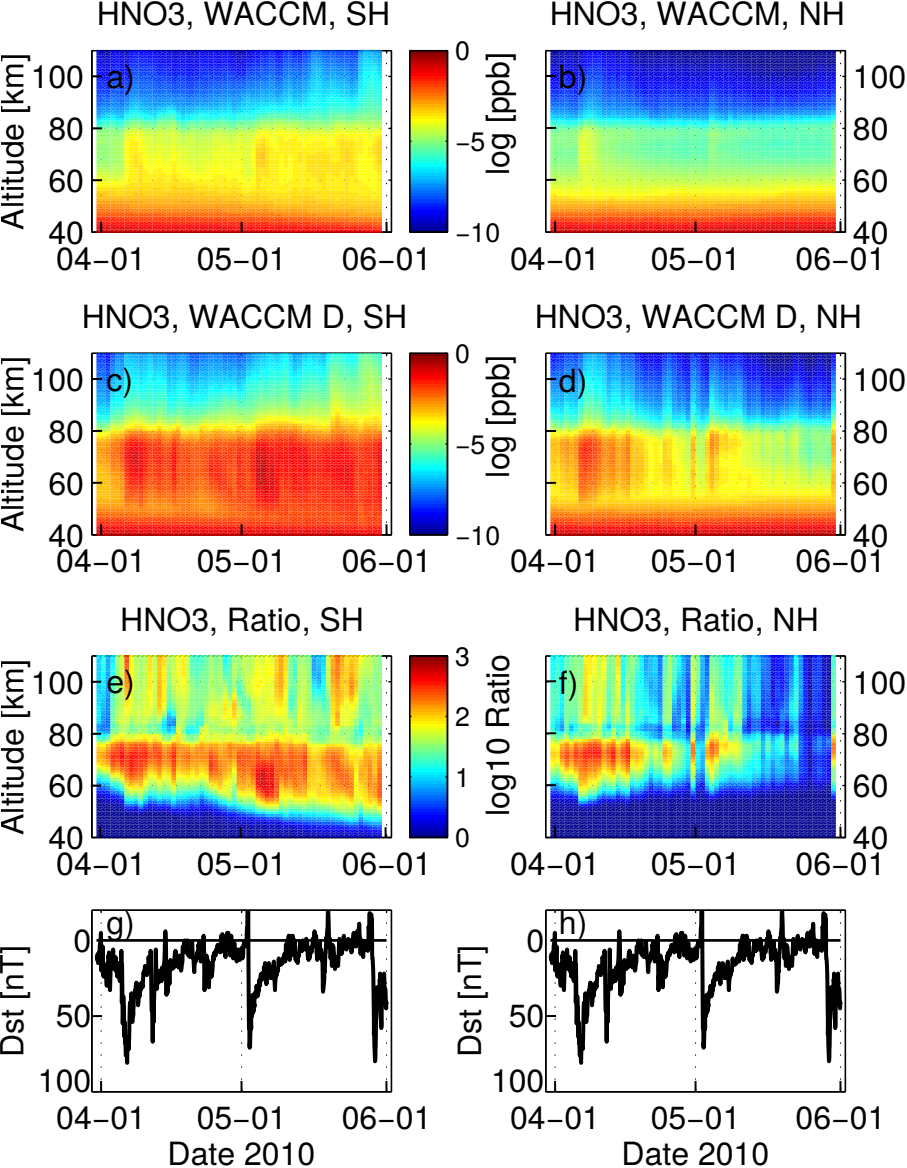
HNO3, WACCM, SH
HNO3, WACCM, NH
HNO3, WACCM D, SH
HNO3, WACCM D, NH
HNO3, Ratio, SH
HNO3, Ratio, NH
a)
b)
c)
d)
e)
f)
g)
h)
Altitude [km]
log [ppb]
log10 Ratio
Dst [nT]
Date 2010
04−01
05−01
06−01
40
60
80
100
0
−5
−10
1
2
3
50

Figure 6.

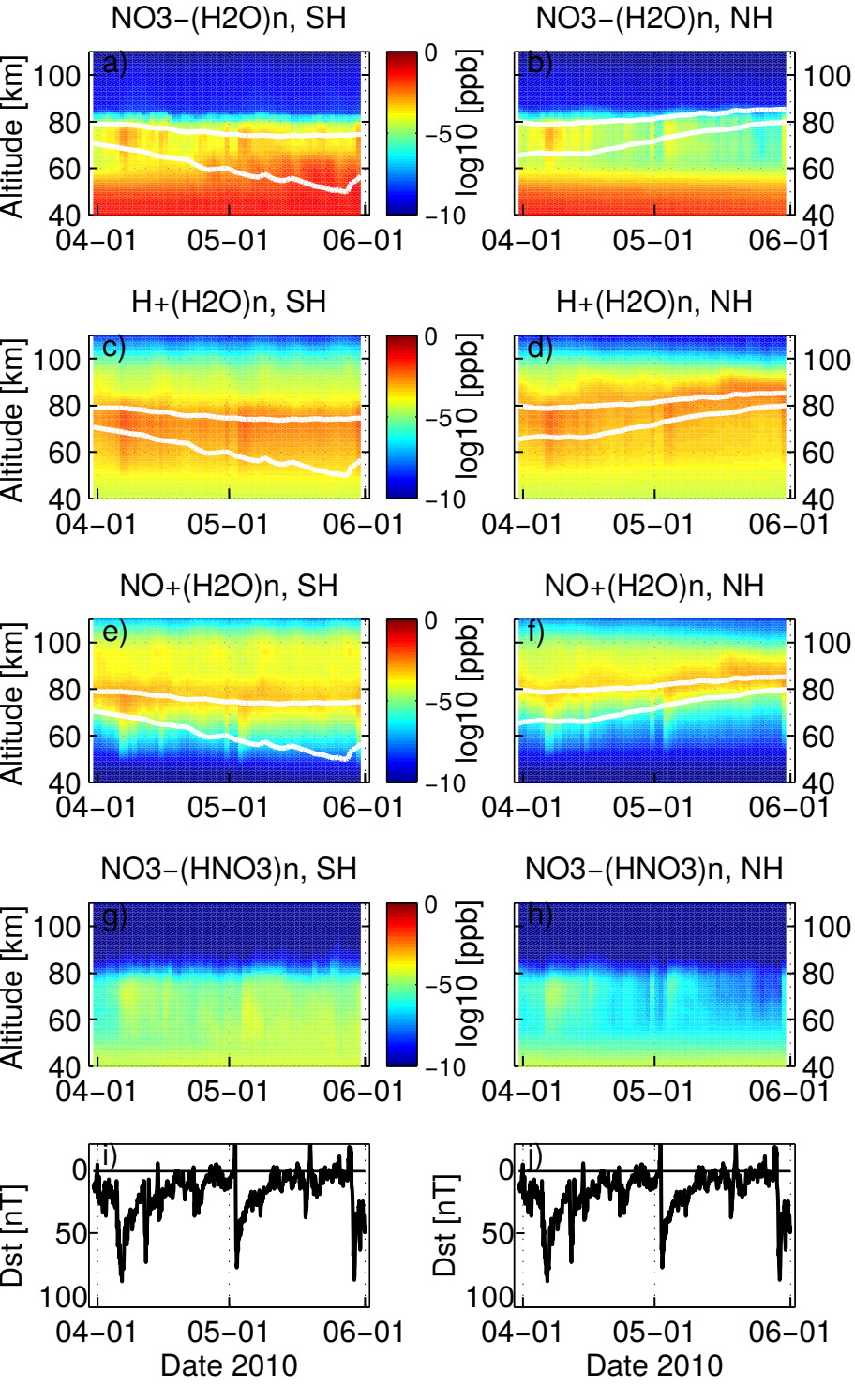
NO3−(H2O)n, SH
NO3−(H2O)n, NH
H+(H2O)n, SH
H+(H2O)n, NH
NO+(H2O)n, SH
NO+(H2O)n, NH
NO3−(HNO3)n, SH
NO3−(HNO3)n, NH
a)
b)
c)
d)
e)
f)
g)
h)
i)
j)
Altitude [km]
log10 [ppb]
Dst [nT]
04−01
05−01
06−01
Date 2010

Figure 7.

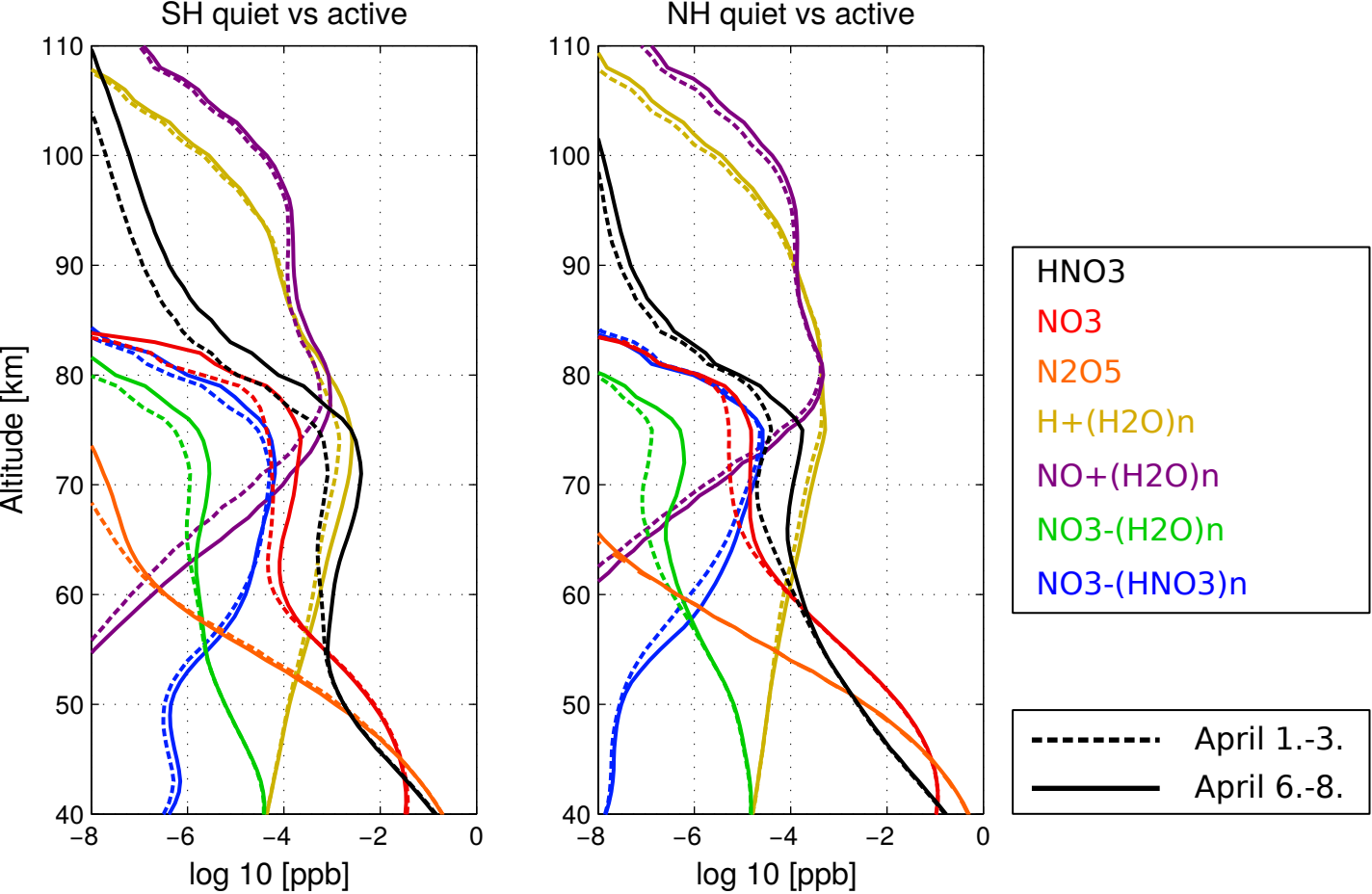
SH quiet vs active
NH quiet vs active
Altitude [km]
110
100
90
80
70
60
50
40
−8
−6
−4
−2
0
log 10 [ppb]
HNO3
NO3
N2O5
H+(H2O)n
NO+(H2O)n
NO3-(H2O)n
NO3-(HNO3)n
April 1.-3.
April 6.-8.

Figure 8.

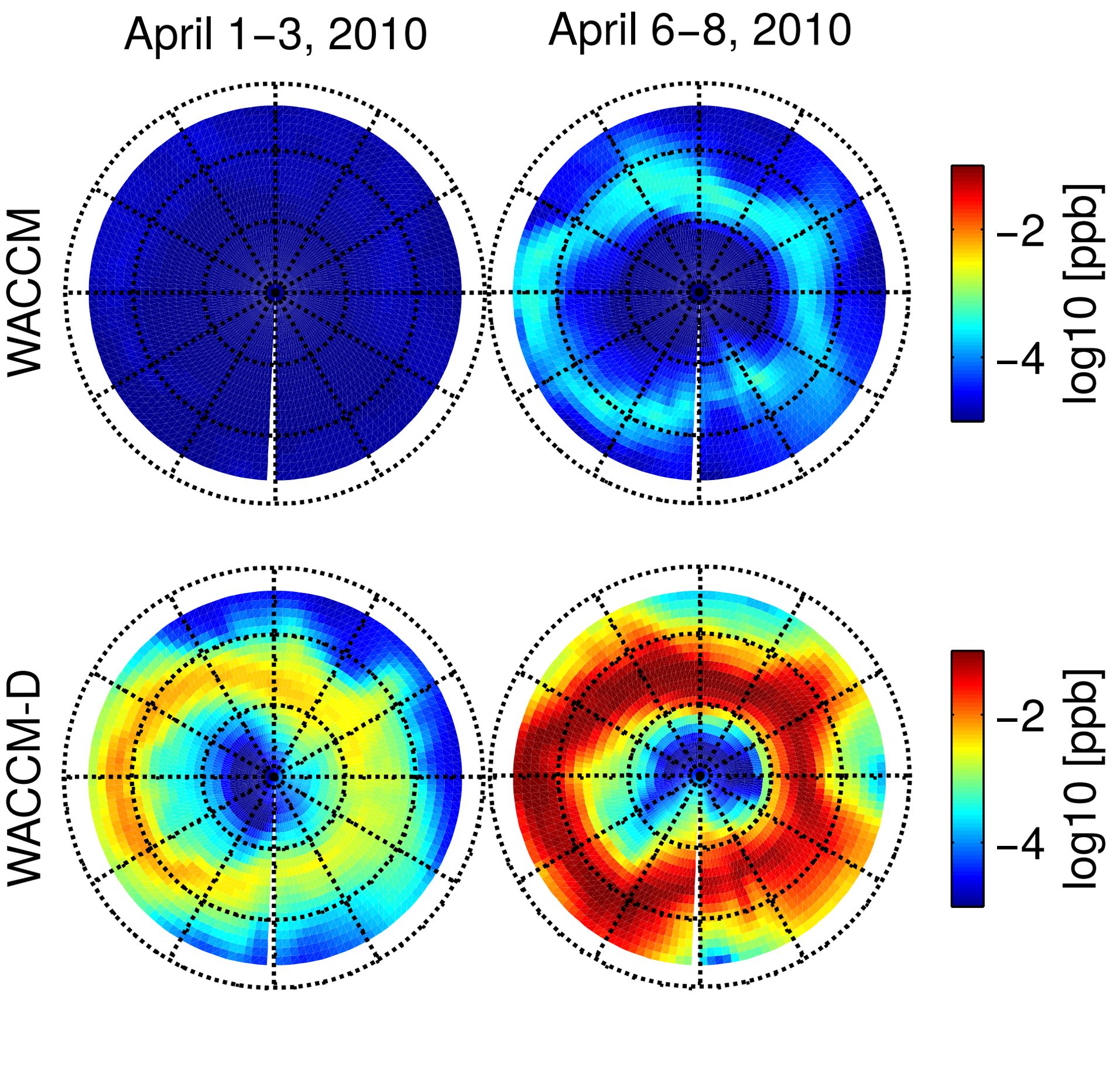
April 1–3, 2010
April 6–8, 2010
WACCM
WACCM-D
−2
−4
log10 [ppb]
−2
−4
log10 [ppb]

Figure 9.

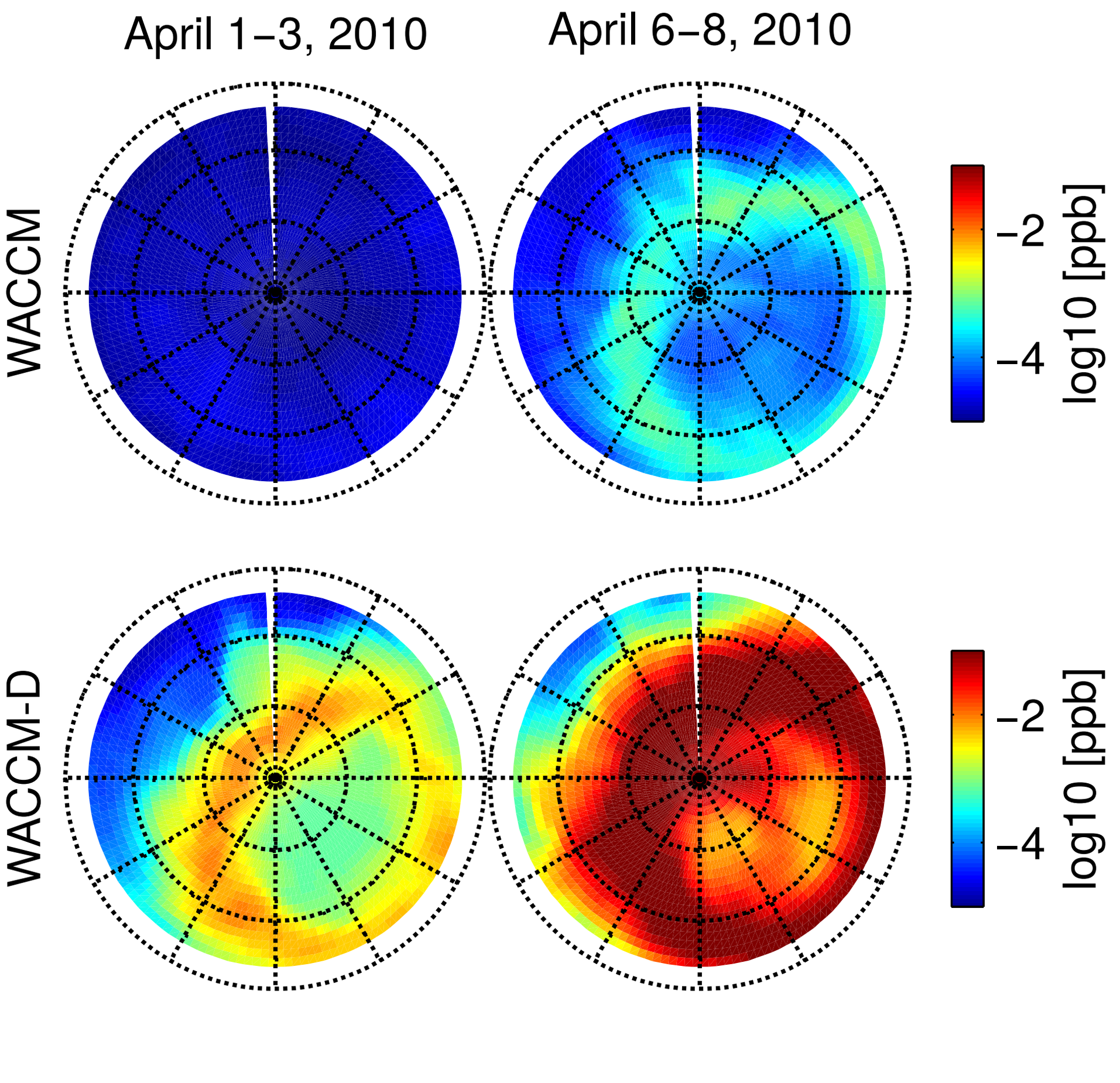
April 1–3, 2010
April 6–8, 2010
WACCM
WACCM-D
−2
−4
log10 [ppb]
−2
−4
log10 [ppb]

Figure 10.

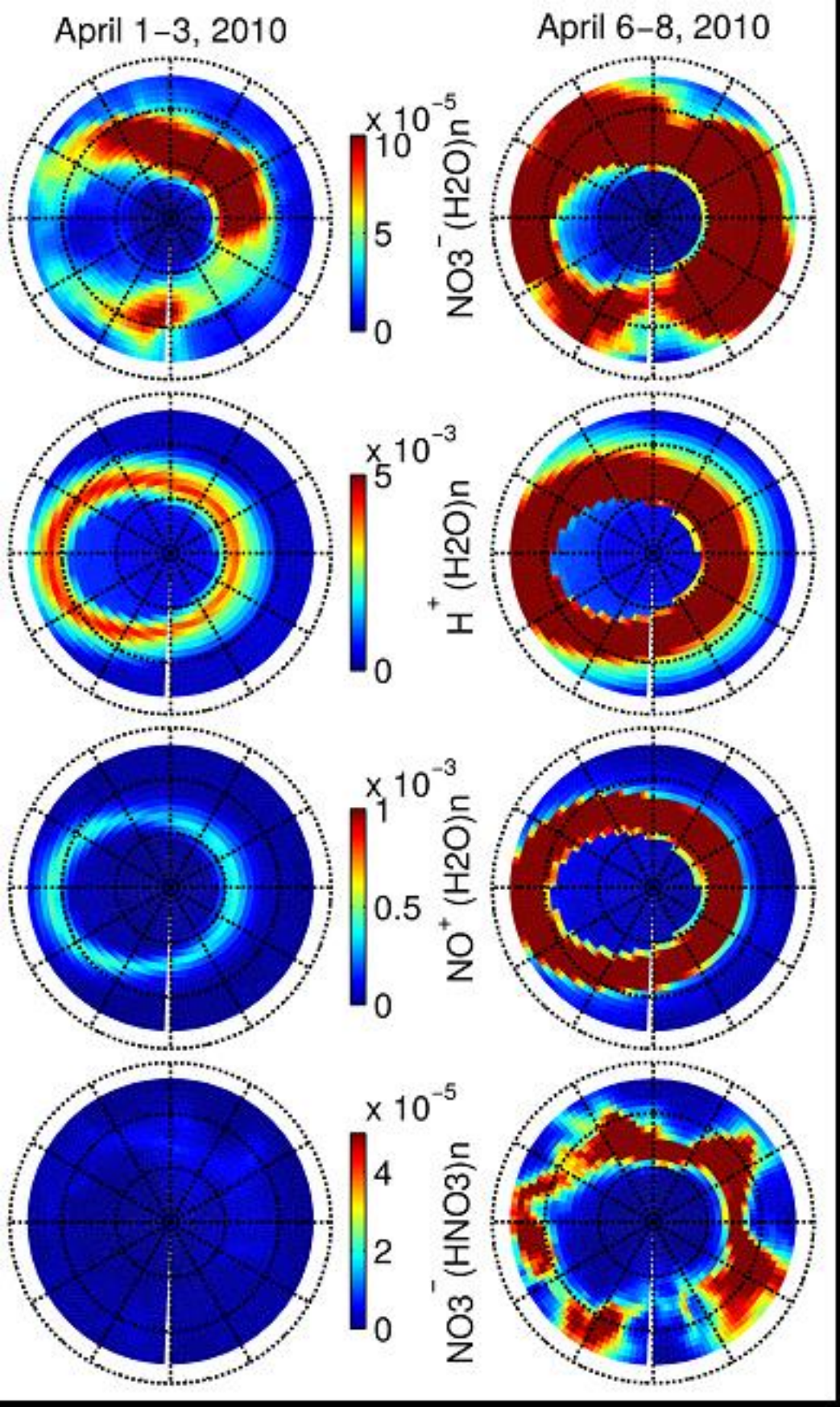
April 1–3, 2010
April 6–8, 2010
x 10^-5
10
5
0
NO3^-(H2O)n
x 10^-3
5
0
H^+(H2O)n
x 10^-3
1
0.5
0
NO^+(H2O)n
x 10^-5
4
2
0
NO3^-(HNO3)n

Figure 11.

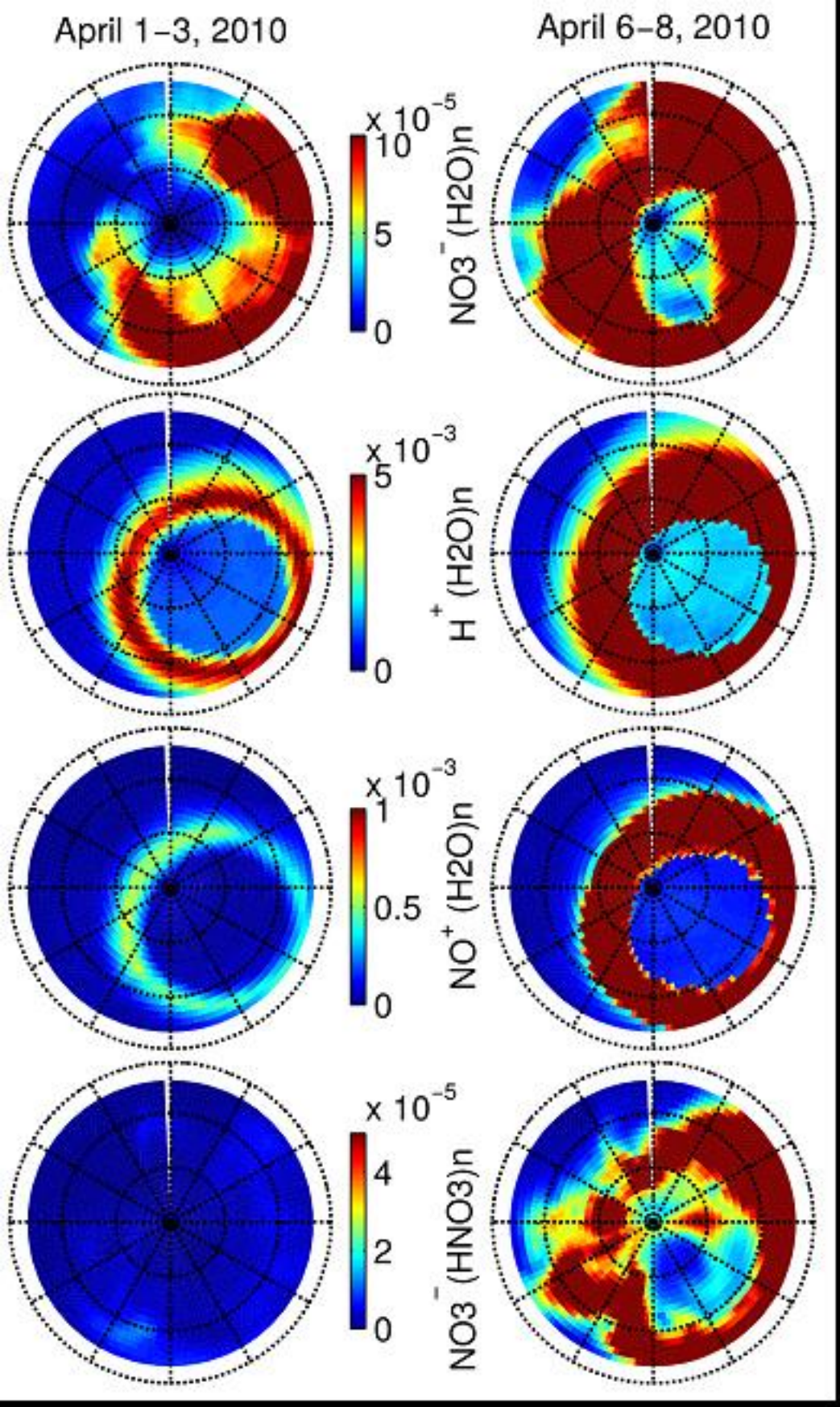
April 1–3, 2010
April 6–8, 2010
x 10^-5
10
5
0
NO3^- (H2O)n
x 10^-3
5
0
H^+ (H2O)n
x 10^-3
1
0.5
0
NO^+ (H2O)n
x 10^-5
4
2
0
NO3^- (HNO3)n

Figure 12.

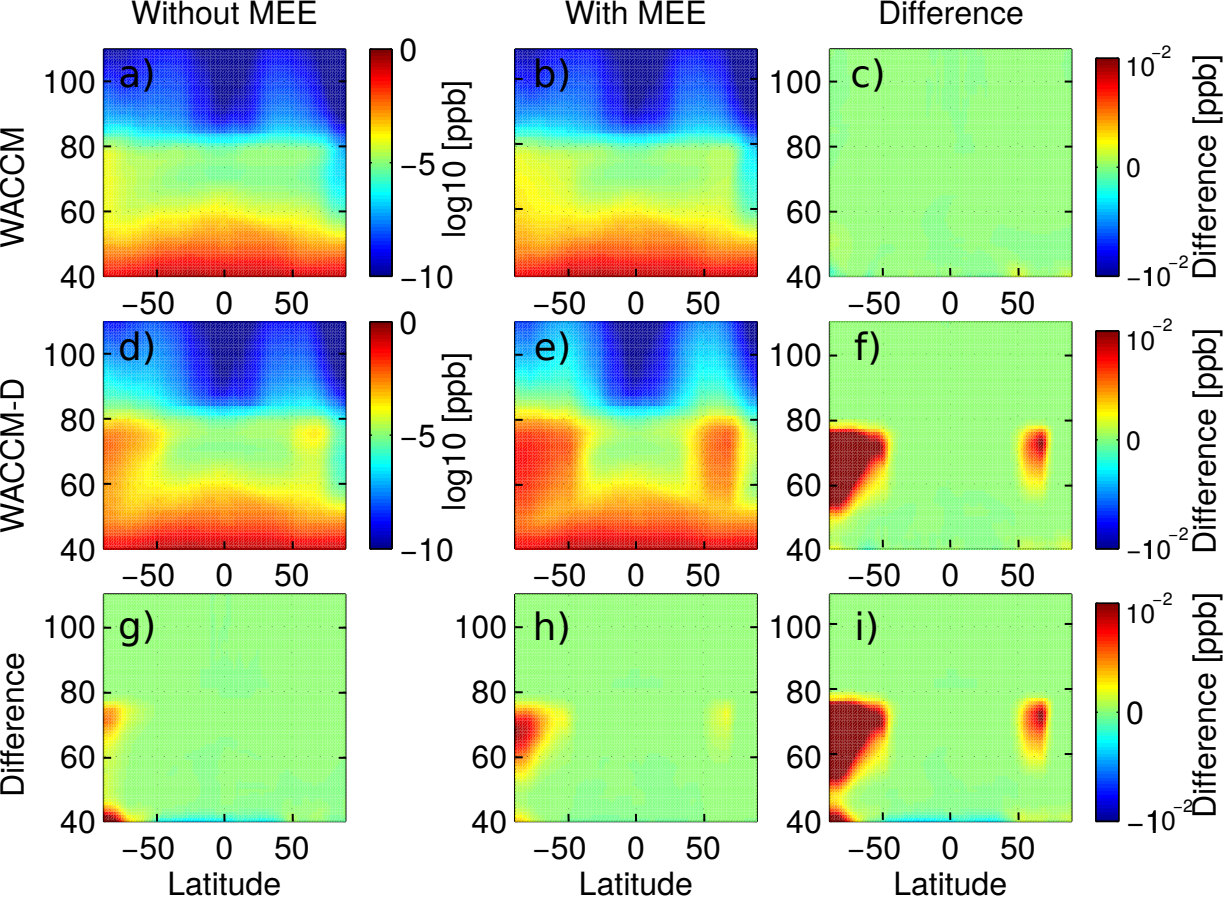
Without MEE
With MEE
Difference
WACCM
WACCM-D
Difference
a)
b)
c)
d)
e)
f)
g)
h)
i)
log10 [ppb]
Difference [ppb]
Latitude
100
80
60
40
−50
0
50
0
−5
−10
10^{-2}
-10^{-2}

Figure 13.

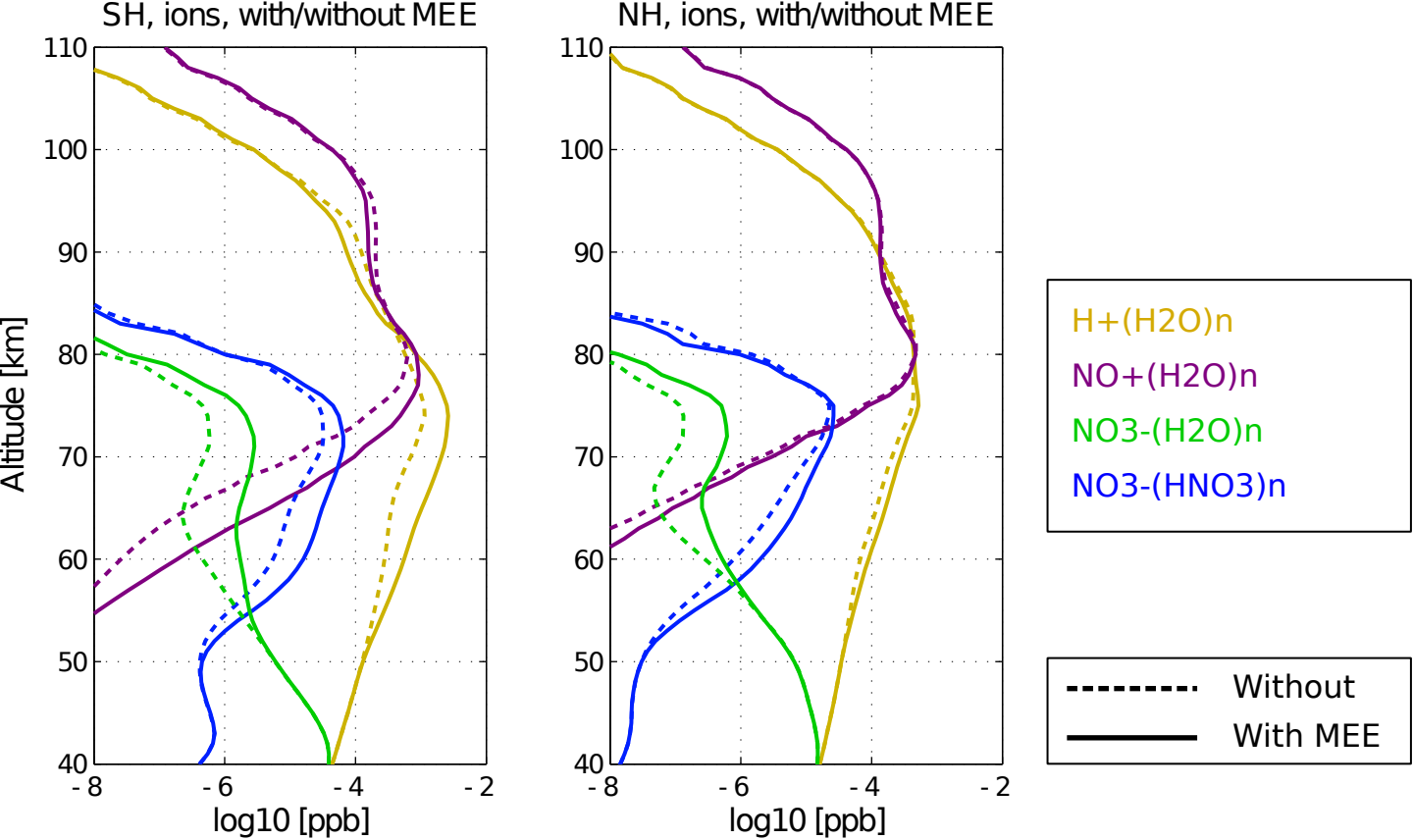
SH, ions, with/without MEE
NH, ions, with/without MEE
Altitude [km]
110
100
90
80
70
60
50
40
- 8
- 6
- 4
- 2
log10 [ppb]
H+(H2O)n
NO+(H2O)n
NO3-(H2O)n
NO3-(HNO3)n
Without
With MEE